Dust Emission Inversion Using Himawari-8 AODs Over East Asia
An Extreme Dust Event in May 2017

Jin, Jianbing; Segers, Arjo; Heemink, Arnold; Yoshida, Mayumi ; Han, Wei; Lin, Hai Xiang

DOI
10.1029/2018MS001491

Publication date
2019

Document Version
Final published version

Published in
Journal of Advances in Modeling Earth Systems

JAMES | Journal of Advances in Modeling Earth Systems

RESEARCH ARTICLE
10.1029/2018MS001491

Dust Emission Inversion Using Himawari-8 AODs Over East Asia: An Extreme Dust Event in May 2017

Jianbing Jin[1], Arjo Segers[2], Arnold Heemink[1], Mayumi Yoshida[3], Wei Han[4], and Hai-Xiang Lin[1]

[1]Delft Institute of Applied Mathematics, Delft University of Technology, Delft, Netherlands, [2]Department of Climate, Air and Sustainability, TNO, Utrecht, Netherlands, [3]Earth Observation Research Center, Japan Aerospace Exploration Agency, Tsukuba, Japan, [4]Numerical Weather Prediction Center, Chinese Meteorological Administration, Beijing, China

Key Points:
- The dust storm emission inversion is conducted by assimilating the new Himawari-8 AODs with high spatiotemporal resolutions
- A novel dust mask screen-based selection is designed to exclude those less representative AODs
- The estimated dust forecast shows better agreements with independent PM_{10} data

Correspondence to:
J. Jin,
J.Jin-2@tudelft.nl

Citation:
Jin, J., Segers, A., Heemink, A., Yoshida, M., Han, W., & Lin, H.-X. (2019). Dust emission inversion using Himawari-8 AODs over East Asia: An extreme dust event in May 2017. *Journal of Advances in Modeling Earth Systems*, *11*, 446–467. https://doi.org/10.1029/2018MS001491

Received 31 AUG 2018
Accepted 27 JAN 2019
Accepted article online 30 JAN 2019
Published online 12 FEB 2019

Abstract Aerosol optical depths (AODs) from the new Himawari-8 satellite instrument have been assimilated in a dust simulation model over East Asia. This advanced geostationary instrument is capable of monitoring the East Asian dust storms which usually have great spatial and temporal variability. The quality of the data has been verified through a comparison with AErosol RObotic NETwork AODs. This study focuses on extreme dust events only when dust aerosols are dominant; promising results are obtained in AOD assimilation experiments during a case in May 2017. The dust emission fields that drive the simulation model are strongly improved by the inverse modeling, and consequently, the simulated dust concentrations are in better agreements with the observed AOD as well as ground-based observations of PM_{10}. However, some satellite AODs show significant inconsistence with the simulations and the PM_{10} and AErosol RObotic NETwork observations, which might arise from retrieval errors over a partially clouded scene. The data assimilation procedure therefore includes a screening method to exclude these observations in order to avoid unrealistic results. A *dust mask* screening method is designed, which is based on selecting only those observations where the deterministic model produces a substantial amount of dust. This screen algorithm is tested to give more accurate result compared to the traditional method based on background covariance in the case study. Note that our screen method would exclude valuable information in case the model is not able to simulate the dust plume shape correctly; hence, applications in related studies require inspections of simulations and observations by user.

1. Introduction

East Asia is affected by severe dust storms every year, especially in late spring and early summer. These dust storms usually originate from the Mongolia and Gobi Deserts and then move to the densely populated eastern areas of China by the prevailing winds. Occasionally, the dust clouds even reach the Korean peninsula and Japan. Though those dust events only last for a few days, they carry a great amount of dust aerosols to the downwind regions. The substantial dust particles not only pose great threats to human health and social activities but also influence the atmospheric environments and biochemistry (Calil et al., 2011; Shao & Dong, 2006; Wu et al., 2016).

To understand the formation and spread of dust, simulation models have been developed that describe the dust life cycle of emission, transport, and deposition (Gong et al., 2003; Liu et al., 2003; Wang et al., 2000). Those models not only help us to better understand the characteristics of the dust storms but also are essential elements of dust forecasting and early warning systems. However, huge discrepancies usually exist in simulated dust concentrations even in case the different modeling systems use the same dust emission parametrization scheme, boundary conditions, and meteorological data (Huneeus et al., 2011; Niu et al., 2008). It is also reported that the differences between dust simulations and real observations can be as large as 2 orders of magnitudes. The uncertainty in the dust emission modeling is the main reason for such large differences (Gong & Zhang, 2008; Uno et al., 2006). The high levels of uncertainties in dust emission parametrization are due to insufficient knowledge about the dust lifting itself, the lack of input data on the soil characteristics and the impossibility for the models to resolve the fine-scale variability in wind fields that drive the dust emission (Escribano et al., 2016; Foroutan & Pleim, 2017; Foroutan et al., 2017).

Data assimilation provides a method to feed measurements into the dynamic models, in order to improve the estimate of the model state or its input parameters. In the dust data assimilation field, both the variational data assimilation methods and ensemble-based filtering have been adopted to assimilate the available observations. Surface visibility and aerosol optical depth (AOD) were incorporated into the China Unified Atmospheric Chemistry Environment/Dust to correct the errors in initial conditions by three-dimensional variational data assimilation (Gong & Zhang, 2008; Niu et al., 2008; Wang et al., 2008; Zhou et al., 2008). In that work, a relationship between PM_{10} observations and visibility was established, which transferred the large number of visibility monitoring data into dust concentrations. Lin, Wang, and Zhu (2008a) and Lin, Zhu, and Wang (2008b) assimilated daily averaged PM_{10} using an Ensemble Kalman Filter, which also resulted in corrected initial model states.

In addition to the state variable estimation, the emission inversion from observations is also an important research topic in dust modeling. Yumimoto et al. (2008) assimilated AOD observations from ground-based LIDAR sites to estimate the dust emission rate using four-dimensional variational (4DVar) data assimilation. Aerosol products from the MODIS instrument have also been used widely in dust/aerosol emission inverse modeling by ensemble-based (Di Tomaso et al., 2017; Khade et al., 2013; Schutgens et al., 2012; Yumimoto et al., 2016) and variational data assimilation (Escribano et al., 2016; Yumimoto & Takemura, 2015). While those AOD observations only provide information about the total column, satellite observations from the CALIPSO instrument provide information on the vertical structure of a dust plume. Those measurements are also used to estimate the emission field using Local Ensemble Transform Kalman Filter (Sekiyama et al., 2010). Recently, dust emission inversion was conducted by Jin et al. (2018), in which the hourly measured PM_{10} measurements from the observing network established by the China Ministry of Environmental Protection (MEP) are assimilated using a reduced tangent linearization (RTL) 4DVar. In that work, model reducing techniques were designed which significantly reduce the computation cost of building the tangent linear model. Also, an observational bias correction algorithm was designed to exclude the nondust fraction from the PM_{10} concentration which made the PM observations more representative.

The observations of AOD and particulate matter (PM) are of high importance for improving dust simulations. However, the limitations are also not negligible. For instance, the ground-based stations that observe visibility, PM_{10}, or AOD are often located only in the downwind and densely populated regions, which are far away from the source regions of dust in East Asia (the Mongolia and Gobi Deserts). Those instruments can only measure the dust levels when the plumes have already arrived in the downwind areas; hence, they are of little help to the early dust forecasting and warning system. Besides, the model error due to the transport process usually grows with the distance that the plume travels. Even in case the dust emissions would be known accurately, the simulation error could be substantial by the time that the plume reaches an observation site. It will then be difficult to determine whether the simulation-observation differences are due to the transport error or the emission deficiencies. Satellite instruments such as CALIPSO or MODIS are better capable of measuring the dust plume at its initial stage. However, CAPLISO has a narrow spatial coverage of about 5 km and therefore only a limited observing coverage. The MODIS products provide a much larger spatial coverage but only information on the total column and therefore no estimate of the plume height or thickness. The polar orbiting instruments also have a limited temporal coverage; for example, the MODIS AQUA and TERRA platforms pass by only around 10:30 and 13:30 (local time).

Designed with the wide observing coverage and high temporal resolution, geostationary measuring instruments provide valuable information to track these short-term and fast-changing airborne pollution events. Such as Seviri carried onboard Meteosat Second Generation, the aerosol products have been used in dust storm detection (Ian & Richard, 2012) over North Africa and volcanic ash estimation (Fu et al., 2017) in Europe. The first of the next-generation geostationary Earth orbit meteorological satellites, Himawari-8, was launched in October 2014 by the Japan Meteorological Agency (Bessho et al., 2016) and is pointed to East Asia. One of the instruments on the satellite is the Advanced Himawari Imager (AHI), which has significantly higher radiometric, spectral, and spatial resolution than those previously available in the geostationary orbit. The AHI has a multiband imager with 16 spectral channels, covering a wavelength range from 0.46 to 13.3 μm. With a short observation interval of 10 min for the full disk and 2.5 min for specific target regions, Himawari-8 has the ability to track fast-changing phenomena and thus provide useful data for assimilation into a dust storm model over East Asia. The Himawari-8 aerosol properties have already been used in the airborne aerosol data assimilation (Yumimoto et al., 2016) and also in the dust

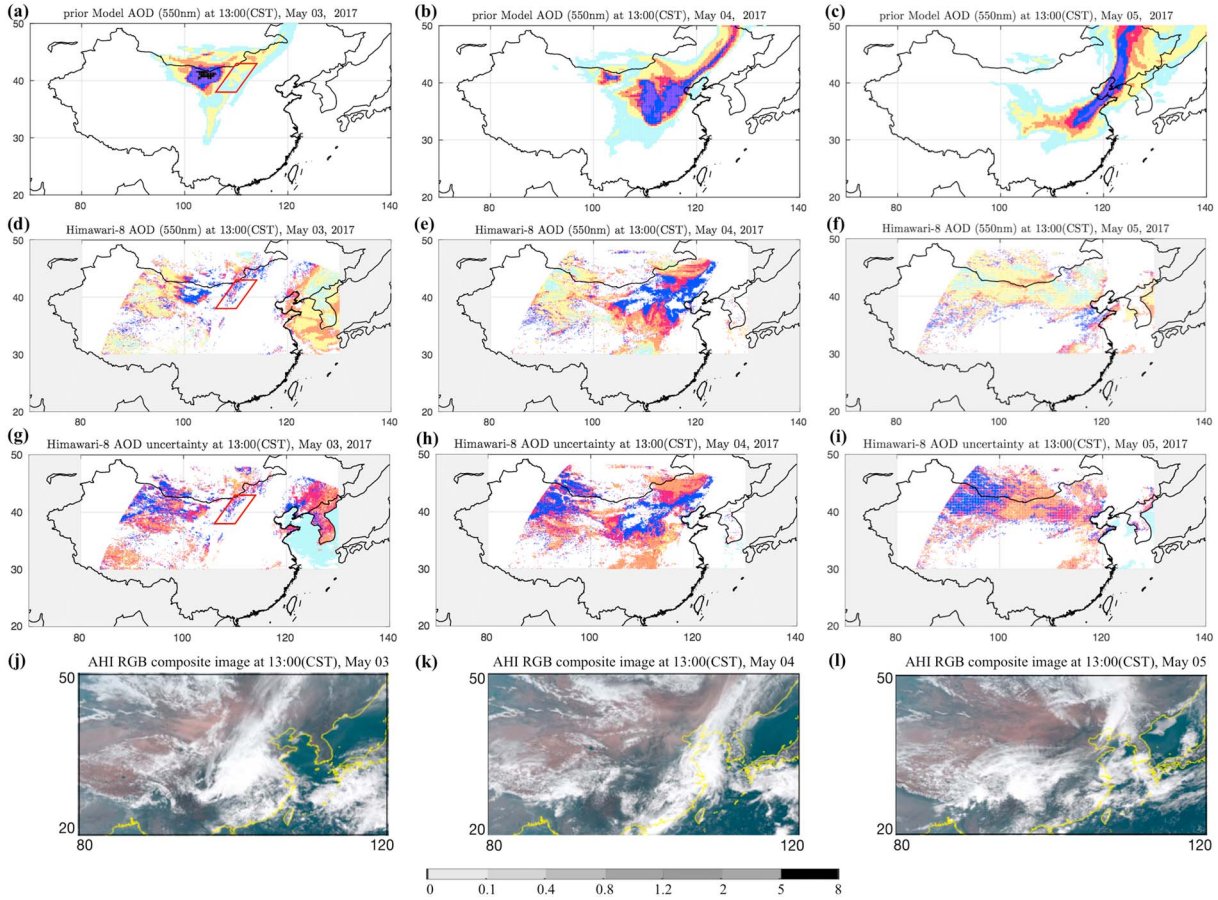

Figure 1. Simulations of AOD (550 nm) by LOTOS-EUROS model, as well as Himawari-8 AOD (550 nm), and AOD uncertainty and AHI RGB composite image at 13:00 (CST), 3 to 5 May. (a–c) Model AOD. (d–f) Himawari AOD. (g–i) Himawari AOD uncertainty. (j–l) AHI RGB image. AHI = Advanced Himawari Imager; RGB = red green blue.

data assimilation which shows the overwhelming strength compared to the MODIS satellite measurements (Sekiyama et al., 2016).

In this paper, we present the dust emission inversion using AOD observations from the Himawari-8 instrument. The geostationary satellite potentially covers both the dust source regions and the dust-affected regions, with high spatial and temporal resolution. This opens the possibility that a dust storm is observed in an early stage already and could therefore help to reduce the uncertainty in the emission estimate. The observations are assimilated into a dust simulation model based on the LOTOS-EUROS chemistry transport model using the RTL 4DVar technique (Jin et al., 2018). To ensure that the Himawari observations and model simulations are consistent with each other, special attention is paid to the observation selection. A dust masking technique that only selects observations where the model is able to simulate a dust load has been developed too.

A description of the dust simulation model (LOTOS-EUROS) is provided in section 2, together with simulation results for the extreme dust storm event over China that has been selected as test case. In section 3, the background uncertainties in the dust emission with respect to the wind field and friction velocity threshold are analyzed. The methodology of the RTL 4DVar is described in section 4. The Himawari-8 AODs used for data assimilation are described and evaluated using the ground-based AOD observations from the AErosol RObotic NETwork (AERONET) network in section 5. This section also describes the ground-based observation network from the China MEP that is used to provide independent PM_{10} data to assess the dust simulations. In section 6, both the *dust mask* (DM) observation screen method and a traditional measurement selection method are described and illustrated. Assimilation results are then shown and evaluated by comparisons with the available AOD and PM_{10} observations in section 7.

2. Dust Simulation Model

2.1. LOTOS-EUROS Model

The LOTOS-EUROS regional chemistry transport model is used to simulate the dust storms over East Asian areas. It has been widely used in the daily air quality forecast over Europe (Manders et al., 2017) and China (https://www.marcopolo-panda.eu; Timmermans et al., 2017) and also for dust emission data assimilation in East Asia (Jin et al., 2018). In this study, the model only simulates dust, since the focus is on estimation of dust emissions for a case with an extreme dust storm event in northeast China. Although in urbanized areas in this region the amount of nondust aerosol could be substantial too, for the event that is studied, these amounts are relatively small compared to the observed dust concentration. The nondust aerosol is therefore neglected here but might become important when the focus changes to the analysis of long time series of Himawari data during episodes where dust is less present.

To establish a dust simulation system over the East Asia areas, the LOTOS-EUROS model is configured on a domain from 15°N to 50°N and 70°E to 140°E (Figure 1), with a resolution about 0.25° × 0.25°. Vertically, the model consists of eight mixing layers with a top at 10 km. The model is driven by the European Center for Medium-Ranged Weather Forecast operational forecasts for forecast horizons of 3–12 hr, starting from the 00:00 and 12:00 analyses. The data are extracted from the archive at regular longitude/latitude grid of about 7-km resolution. Physical processes included are advection, diffusion, dry and wet deposition, and sedimentation. The dust load is described by five aerosol bins within a diameter range 0.01 μm < D_p < 10 μm. Similar aerosol size range setting can be found in dust model NMMB-MONARCH (Di Tomaso et al., 2017) and BSC-DREAM8b (Mona et al., 2014).

2.2. Dust Storm Event

In this paper, a dust storm event is investigated that occurred in May 2017. This dust event is reported to be the most severe one in the past 20 years. Figures 1a–1c show the LOTOS-EUROS simulation of AOD (550 nm) at 13:00 (CST) for 3 to 5 May. The model AOD map on 3 May shows that the severe dust plume stayed in Inner Mongolia, while a very small part was already transported to Central China. In the most severe dust plume, the maximum model AOD value was around 5 to 8. In the next 24 hr, the main plume was gradually blown along the southeast direction. The area affected by the dust storm is extended, while the maximum simulated column-integrated AOD lowers to a range from 2 to 5. On 4 May 13:00, the dust plume covers almost all of North China, and a new dust plume started to develop in Inner Mongolia. In the third day, most of north China is free of extreme dust loads, and the main plume has been transported further to the south east and even arrived at the Korean Peninsula. The dust aerosols deposited significantly while the plume moved to the east, and most of the simulated AOD values are lower than 2 on 5 May, 13:00.

3. Uncertainty in Dust Emissions

The goal of this study is to estimate dust emissions during a severe dust event by assimilation of Himawari-8 AOD observations. To achieve this, it is necessary to describe the uncertainty in the dust simulations. We assume that the main uncertainty is in the parametrization of the dust emissions. Although other model elements such as transport and deposition are uncertain too, for the event under study they are assumed to be of less importance than the location and the amount of dust emission. This assumption could be seen as a first step toward a system that takes into account other uncertainties too but that probably requires additional information such as vertical distributions of the dust load which are currently not available.

3.1. Emission Parametrization

The dust emission scheme implemented in LOTOS-EUROS is mainly based on the formulation of horizontal saltation flux (Marticorena & Bergametti, 1995) and sandblasting efficiency α (Shao et al., 1996). The vertical dust flux f (μg · m^{-2}· s^{-1}) in a given cell is parameterized as follows

$$f(u,u_t)=\begin{cases}0 & u\le u_t\\ C\cdot\alpha\cdot\frac{p_a}{g}u^3\cdot(1+\frac{u_t}{u})(1-\frac{u_t^2}{u^2}) & u>u_t\end{cases} \quad (1)$$

where u denotes the wind friction velocity while u_t represents the friction velocity threshold. Only when u overcomes the minimum erosive force to initialize the soil particles' motion, the dust emission occurs. C is the fraction of the erodible surface in the given cell; surface covered with snow, vegetation, or water is classified as nonerodible land and excluded from the potential dust source list. In the previous work (Jin et

al., 2018), we have shown that the error in the friction velocity threshold parametrization is one of the main reasons that prohibits accurate dust forecasts. Besides, the wind field uncertainty itself will also introduce uncertainty in the emission, as f is proportional to the cube of u.

3.2. Emission Uncertainty

For the data assimilation algorithm described in section 4, both the background emission field and its uncertainty are required. The latter defines the distribution of the deviation from the former. Considering the main drivers of the emission, the emission deviation can be approximated as a linear combination of these two parameters, friction velocity and friction velocity threshold

$$\delta f \approx F_u \, \delta u + F_{u_t} \delta u_t \tag{2}$$

The linear operators F_u and F_{u_t} approximate the change in emissions given changes in u and u_t with respect to a simulation with the default configuration. We assume that the uncertainty in the friction velocity δu (which is a property of the meteorology) is independent from the uncertainty in the friction velocity threshold δu_t (which is a property of the soil). Further, we define the vectors $\delta\vec{u}$ and $\delta\vec{u}_t$, which consist of δu and δu_t in the model grid cells, respectively, and assume that their uncertainty follows a Gaussian distribution defined by a zero mean and covariance matrices $\mathbf{B}_u$ and $\mathbf{B}_{u_t}$, respectively. The uncertainty in the vector $\delta\boldsymbol{f}$ with emission perturbations on the grid is then

$$\mathbf{B} = \mathbf{F}_u \, \mathbf{B}_u \, \mathbf{F}_u^T + \mathbf{F}_{u_t} \, \mathbf{B}_{u_t} \, \mathbf{F}_{u_t}^T \tag{3}$$

with $\mathbf{F}_u$ and $\mathbf{F}_{u_t}$ the matrix operators based on the linearizations. To perform a proper orthogonal decomposition (POD) of the error covariance $\mathbf{B}$ in the RTL 4DVar, which will be described in more detail in section 4, more efficient, parameter filters (Jin et al., 2018) are used. In this study, they significantly reduce the size of the emission vector $\vec{f}$ to $O(10^4)$ by excluding those nonsensitive emissions.

The emission covariance is not exactly computed as in equation (3) which would require the input of the two huge-sized uncertainty matrix, $\mathbf{B}_u$ and $\mathbf{B}_{u_t}$, and the matrix operators $\mathbf{F}_u$ and $\mathbf{F}_{u_t}$. The two contributions to the covariance of the emission deviation are discussed in the following sections 3.3 and 3.4.

3.3. Uncertainty in Friction Velocity

A suitable method to estimate the uncertainty in emissions due to uncertainty in the friction velocity field is to use the variability in the meteorological input. For the European Center for Medium-Ranged Weather Forecast meteorological forecasts that are used as model input, the variability could be estimated from the ensemble forecast that is available too, where each member is a perturbation of the deterministic forecast. For the studied period the ensemble forecast consists of 26 different members, and each of these have been used with the model to compute dust emissions. These ensemble forecasts are valid for prediction horizons of 3–12 hr from the 06:00 and 18:00 analyses, extracted from the archive at a resolution of about 30 km. The ensemble covariance of these emissions is then representative for the uncertainty in the emissions due to uncertainty in friction velocity

$$\mathbf{F}_u \, \mathbf{B}_u \, \mathbf{F}_u^T \approx \frac{1}{N_1 - 1} \sum_{k=1}^{N_1} \left(\vec{f}_{u,k} - \bar{\vec{f}}_u \right) \left(\vec{f}_{u,k} - \bar{\vec{f}}_u \right)^T \tag{4}$$

where $\vec{f}_{u,k}$ denotes the emission vector computed using meteorological ensemble member k, $\bar{\vec{f}}_u$ is the ensemble average, and $N_1 = 26$ is the ensemble size. This ensemble covariance is not computed and stored as a full matrix due to its huge size; instead, the ensemble members are stored and elements of the covariance are evaluated when needed.

3.4. Uncertainty in Friction Velocity Threshold

The parameterization of u_t follows the concept of adding two correction terms to the threshold friction velocity over an idealized dry and smooth surface. One term is for soil moisture, governed by the inputs of soil moisture and soil clay mass fraction, and another one is for the nonerodible surface roughness elements, governed by the input of the surface roughness. The imperfect spatial distributed surface states and soil texture data set are the main reasons for inaccurately modeling the friction velocity threshold in the dust

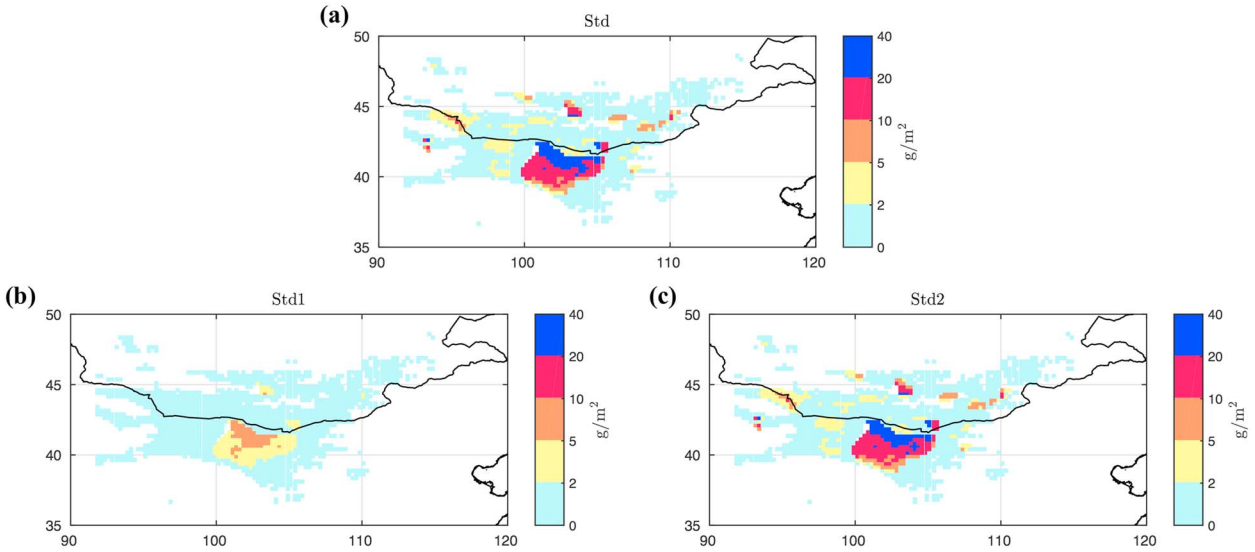

Figure 2. (a) Standard deviation (Std) of the emission index F from 2 May 15:00 to 4 May 15:00. (b) Std of F due to the perturbation in wind field and (c) in friction velocity threshold map.

emission parametrization. It is shown in Jin et al. (2018) that the error in the friction velocity threshold can be compensated by introducing a spatially varying multiplicative factor β

$$u_t^{\text{true}}(i,t) = \beta(i) \cdot u_t(i,t) \tag{5}$$

where $u_t(i,t)$ is the model parameterized friction velocity threshold in a given cell i at time t and u_t^{true} is the true value. The β factors are defined to be temporally constant within each assimilation cycle. The values are defined to be random variables with a mean of 1.0 and a standard deviation $\sigma = 0.1$, with a truncation to the interval [0.7,1.3] to avoid extreme variations. This empirical standard deviation was found to provide sufficient variations to explain the observation-simulation difference. The background covariance of β is formulated as a combination of the constant standard deviation and a correlation matrix $\mathbf{C}$ as follows

$$\mathbf{B}_\beta(i,j) = \sigma^2 \cdot \mathbf{C}(i,j) \tag{6}$$

where the $\mathbf{C}(i,j)$ denotes a distance-based spatial correlation between the βs in two grid cells i and j, which is defined as

$$\mathbf{C}(i,j) = e^{-(d_{i,j}/L)^2/2} \tag{7}$$

where $d_{i,j}$ represents the distance between two grid cells i and j. In Jin et al. (2018), the correlation length scale L was configured to be 800 km, which was found to be suitable to simulate the main characteristics of the dust event studied there. In this study, however, a smaller length scale $L = 200$ km is used which gives a higher spatial degree of freedom, while it can still be resolved by the assimilation due to the larger amount of (spatially distributed) satellite data.

With the covariance matrix $\mathbf{B}_\beta$, an ensemble of samples of β is drawn with a random generator. These ensemble samples are then applied in the dust model, and each of them produces a emission forecast. The covariance of these emission fields is used to approximate the emission uncertainty due to the friction velocity threshold

$$\mathbf{F}_{u_t}\,\mathbf{B}_{u_t}\,\mathbf{F}_{u_t}^T \approx \frac{1}{N_2-1}\sum_{k=1}^{N_2}\left(\vec{f}_{u_t,k} - \bar{\vec{f}}_{u_t}\right)\left(\vec{f}_{u_t,k} - \bar{\vec{f}}_{u_t}\right)^T \tag{8}$$

where $\vec{f}_{u_t,k}$ represents the emission vector computed using friction velocity threshold ensemble member k, $\bar{\vec{f}}_{u_t}$ is the ensemble average, and $N_2 = 100$ is the friction velocity threshold sample size.

3.5. Comparison of Uncertainties

To estimate the relative importance of the two contributions to the emission uncertainty, an emission integration index F_i (g/m^2) is computed that represents the accumulated dust emission in a cell i from 2 May 15:00 to 4 May 15:00, the period of which exactly covers the two assimilation cycles as shown in Figure 3. The map of deterministic F_i can be found in Figure 9a, and Figure 2a presents the evaluated standard deviations from the parameterized uncertainties based on the meteorological ensemble and samples of β factors drawn with a random generator over the potential source region. The maps show that the variability in emissions due to uncertainty in friction velocity Figure 2b is small compared to the variability due to uncertainty in friction velocity threshold Figure 2c. The total standard deviation is therefore mainly caused by the uncertain soil parameters in this study case. However, the uncertainty in the wind field might have considerable contribution to the emission uncertainty during other dust storms.

4. RTL 4DVar

4.1. Data Assimilation Methodology

The assimilation system that will be used to combine Himawari-8 AOD observations with the dust simulations is based on a RTL 4DVar. In this study, the goal of the 4DVar technique is to find the maximum likelihood estimator of the dust emission field $\vec{f}$, given the available observations over an assimilation window. A common approach is to use an incremental formulation, which aims to find the optimal emission deviation $\delta\vec{f}$ as the minimum of the cost function

$$J(\delta\vec{f}) = \frac{1}{2} \quad \delta\vec{f} \quad \mathbf{B}^{-1} \quad \delta\vec{f} + \frac{1}{2}\sum_{i=1}^{k}\left(\mathbf{H}_i\mathbf{M}_i\delta\vec{f} + \vec{d}_i\right)^T\mathbf{R}_i^{-1}\left(\mathbf{H}_i\mathbf{M}_i\delta\vec{f} + \vec{d}_i\right) \tag{9}$$

where k is the number of time steps within the assimilation window for which observations are available. For an observation time i, the innovation vector (length m_i) is defined as the difference between the simulation and observations

$$\vec{d}_i = \mathcal{H}_i(\mathcal{M}_i(\vec{f})) - \vec{y}_i \tag{10}$$

where $\mathcal{M}_i$ is the LOTOS-EUROS transport model, $\mathcal{H}_i$ is the operator that relates the observations to the model state, and $\vec{y}_i$ is the vector with observations for this time step. The operators $\mathbf{H}_i$ and $\mathbf{M}_i$ denote the linearizations of $\mathcal{H}_i$ and $\mathcal{M}_i$ around the prior state $\vec{f}_b$, respectively. In each outloop minimization process, the posterior state from the last iteration will be treated as the prior for the next iteration, where the linear operators $\mathbf{H}_i$ and $\mathbf{M}_i$, and the innovation vector $\vec{d}_i$ will be updated. The observation error term is weighted by the observation error covariance $\mathbf{R}$, for which the individual elements will be described in section 5.1. The vector $\delta\vec{f}$ denotes a perturbation of the emissions with respect to the background state, and $\mathbf{B}$ is the covariance matrix of this perturbation as defined in equation (3).

One of the main efforts in using this formulation is the use of the linearized model operator $\mathbf{M}_i$. This *tangent linear model* is often a separate model that needs to be maintained and updated next to the full model $\mathcal{M}_i$. To simplify the method, in this study a RTL 4DVar is used. The RTL 4DVar is based on a POD of the background covariance $\mathbf{B}$ which efficiently carries out a model order reduction by identifying the few most energetic modes

$$\begin{aligned}\mathbf{B} &= \mathbf{U}\mathbf{U}^T \approx \tilde{\mathbf{U}}\tilde{\mathbf{U}}^T\\ \delta\vec{f} &\approx \tilde{\mathbf{U}}\delta\vec{w}\end{aligned} \tag{11}$$

where $\mathbf{U} \in \mathbf{R}^{P\times P}$ is the background emission covariance transform, while $\tilde{\mathbf{U}} \in \mathbf{R}^{P\times p}$ is the truncation of $\mathbf{U}$ based on POD. The vector $\delta\vec{w} \in \mathbf{R}^p$ is the transformed vector, P denotes the emission field size of $O(10^4)$, and p is the reduced rank size. In this study, the size of the background covariance $\mathbf{B}$ is $O(10^4 \times 10^4)$. For this case, the computational cost of a *Cholesky* decomposition is still affordable. In case when $\mathbf{B}$ has a much larger dimension, the principle patterns of the emission vector can also be computed using an *Arnoldi* iteration method (Arnoldi, 1951).

With the truncated transform of $\mathbf{B}$, the cost function of the RTL 4DVar is formulated as follows:

$$J(\delta\vec{w}) = \frac{1}{2}\delta\vec{w}^T\delta\vec{w} + \frac{1}{2}\sum_{i=1}^{k}\left(\mathbf{H}_i\tilde{\mathbf{M}}_i\tilde{\mathbf{U}}\delta\vec{w} + d_i\right)^T\mathbf{R}_i^{-1}\left(\mathbf{H}_i\tilde{\mathbf{M}}_i\tilde{\mathbf{U}}\delta\vec{w} + d_i\right) \tag{12}$$

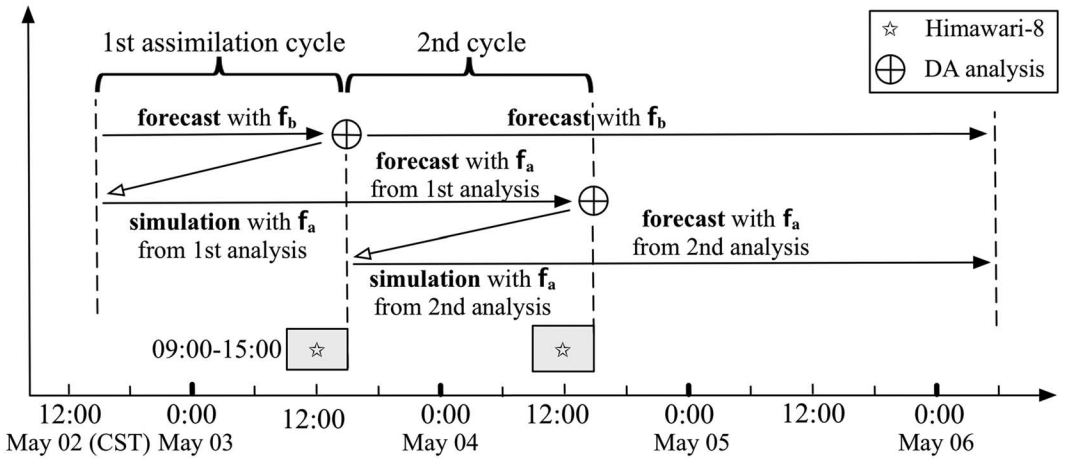

Figure 3. Timeline of observation availability, assimilation windows and forecasts.

where $\tilde{\mathbf{M}}_i$ denotes the reduced tangent linear model with a rank p, which is approximated using the perturbation method. Similar to the traditional incremental 4DVar, posterior control variable vector $\delta\vec{w}$ from the last outer loop iteration will be used as the prior for the next iteration in the minimization process, where both the linear model operator $\tilde{\mathbf{M}}_i$ and innovation $\vec{d}_i$ are updated. In this study, the reduced rank size p is set as 40. A larger reduced rank $p > 40$ is also tested, but the improvement is negligible. By projecting the original parameter field into a subspace of a few leading patterns, the RTL 4DVar significantly decreases the computation time for deriving the linear model operator. However, as it only explores the optimal parameters in a reduced subspace, inevitably some properties of the original dynamic system will be lost. More details about the RTL 4DVar algorithm can be found in Jin et al. (2018).

4.2. Assimilation Window

Figure 3 shows the assimilation window settings for the test event. The dust simulation is configured with a period from 15:00, 2 May, to 06:00, 6 May. The dust outbreak events are fully covered by the assimilation windows; hence, the model is assumed to be free of dust at the starting moment. It forwards with default emission field $\vec{f}_b$ and provides early dust forecast for the whole period if no data assimilation analysis is performed. The first assimilation cycle is set from the start to 15:00, 3 May, with a length of 24 hr, while the available observations from 09:00 to 15:00, 3 May, are used in the RTL 4DVar. Then our model propagates from the start again with the newly estimated emission vector $\vec{f}_a$, resulting in the posterior simulation in the first cycle as well as the dust forecast after 15:00, 3 May. In fact, parts of AOD observations in the following time are also attributed to the dust emission in the first assimilation window; hence, an extended window, for example, 48 hr, will enrich the data to estimate these emissions. However, to provide the in-time dust forecast like in case of an operational system, our assimilation starts once the observations during a full day (09:00–15:00) are obtained.

The second cycle is designed with the same length, and the posterior emission field is used to provide the dust forecast after 15:00, 4 May. After the end of the second cycle, dust emission is negligible and will not be carried into downstream; thus, a third assimilation cycle is not implemented. With the settings of the assimilation window, we are able to evaluate whether the assimilation algorithm helps to improve the dust early forecasting in practical applications.

5. Data for Assimilation and Validation

5.1. Himawari-8 AOD

The Japan Aerospace Exploration Agency (JAXA) has developed a Himawari-8 aerosol retrieval algorithm (Fukuda et al., 2013; Ishida & Nakajima, 2009; Yoshida et al., 2018). Cloud/clear discrimination is performed. The AOD at 500 nm and the Ångström exponent are derived from the visible channels (470, 510, and 640 μm) over land areas and from both the visible (640 μm) and near-infrared data (860 μm) over ocean regions. The JAXA retrievals provide Himawari-8 AOD Level 2 at 10-min intervals with a resolution 0.05° × 0.05°. In this study, the JAXA Himawari-8 Level 2 AOD will be assimilated with the dust simulations using the RTL 4DVar to identify and track the rapid-changing dust storm events.

AOD at the wavelength 550 nm is more widely used to evaluate the aerosol column-integrated concentration; the original Himawari-8 Level 2 products (500 nm) are extrapolated using (Cesnulyte et al., 2014)

$$\mathrm{AOD}_{550} = \mathrm{AOD}_{500} \cdot \left(\frac{550}{500}\right)^{-\alpha} \tag{13}$$

where α represents the Ångström exponent which is also from the Himawari-8 aerosol property product. Figures 1d–1f show three snapshots of the AOD (550 nm) map. For better interpretation, also the RGB composite images from the AHI are shown in Figures 1j–1l. In general, the three plume maps show a large similarity to the prior LOTOS-EUROS AOD simulation as shown in Figures 1a–1c. Note that the Himawari-8 AOD observations do not exceed a value of 2, while the prior model simulated AOD shown in Figure 1a exceeds this value significantly.

As shown in Figure 1d, on 3 May the main part of the dust plume stayed in the boundary region between Mongolia and North China, which is believed to be the source region. The adding value of the Himawari-8 AOD product over ground-based observations is clearly visible for that day, while the dust plume was already observed by the satellite in detail at this early stage, the first ground-based sites that observed the plume are located far away from the source region. For instance, the upstream four sites (Wuhai, Bayanzhuoer, Hohhot, and Baotou) did not measure severe PM_{10} concentration until 4 to 8 hr later (see section 7.3 and Figure 13. The early observations of the dust plume could therefore be of great benefit for a timely forecast of dust storms. Note that only a few AODs are available in the Central China for that day. As shown in the RGB composite in Figure 1j, this region is covered by clouds which hampers retrievals of total AOD columns. The AOD fields retrieved by Himawari have rather high values in an area next to the cloud covered region, which is marked by a red frame in Figure 1d. However, the model simulations did not show high AOD values in this area, and therefore, the high values in the observations might also arise from retrieval errors over a partially clouded scene. The difference between observations and simulations in this region will be discussed further in section 6 on observation selection.

During the next 24 hr, the severe dust plumes were moved southeastward. Figure 1e shows that there was a band with severe dust loads from the Central China to Northeast China around 4 May 13:00 CST. As shown in Figure 1k, the central region of this band is free of cloud, but AOD retrievals there are not available for unknown reasons. A new plume with high dust loads is also present in the Inner Mongolia province. On 5 May, the plume was transported further in southeast direction as shown in Figure 1f and even affected the Korean Peninsula. AOD retrievals over Northeast China are not available on this day, while the model still simulates a band with high dust loads.

Figures 1g–1i represent the AOD uncertainty from the same JAXA Himawari product. The AOD uncertainties over lands stay at a high level similar to the AODs from SEVIRI onboard a geostationary satellite (Carrer et al., 2010) but much larger than the MODIS AODs from polar orbit satellites (Remer et al., 2005). Zhang et al. (2019) indicated they are due to the large uncertainties in the aerosol models and surface reflectance estimation in the retrieval algorithm. In fact, Level 3 with more certain measurements is also available; however, only few AODs survive during the further retrieval hence not used in this work. To make the observation resolution consistent with the model, the Himawari AODs (550 nm) and the uncertainty are coarsened. The coarsened AODs and uncertainty are taken as the average over the $0.25° \times 0.25°$ model grid cell. The coarsened data can be seen in Figure 8.

The square of coarsened uncertainty is set as the diagonals of the observation covariance matrix $\mathbf{R}$. Although the relative uncertainties of the Himawari AODs are higher than the emission uncertainties in Figure 2 with respect to the prior emission in Figure 9, the huge number, $O(10^4 - 10^6)$, due to a fine resolution and a wide coverage still makes the observation error term dominant in the cost function J. In addition, a spatial correlation of the coarse AODs is assumed while building the error matrix $\mathbf{R}$

$$s(i,j) = e^{-a \cdot h(i,j)} \tag{14}$$

where $s(i,j)$ and $h(i,j)$ represent the correlation coefficient and distance between model cells i and j respectively, while $a = 0.03\ \mathrm{km}^{-1}$ is an empirical value based on a statistical analysis of the original Himawari AODs. Note that experiments were also conducted using a diagonal observation error covariance, thus neglecting the spatial correlations in the observation errors. Those assimilation runs resulted in similar results (not included in this paper) to the experiments shown here. This is because that our simulation is

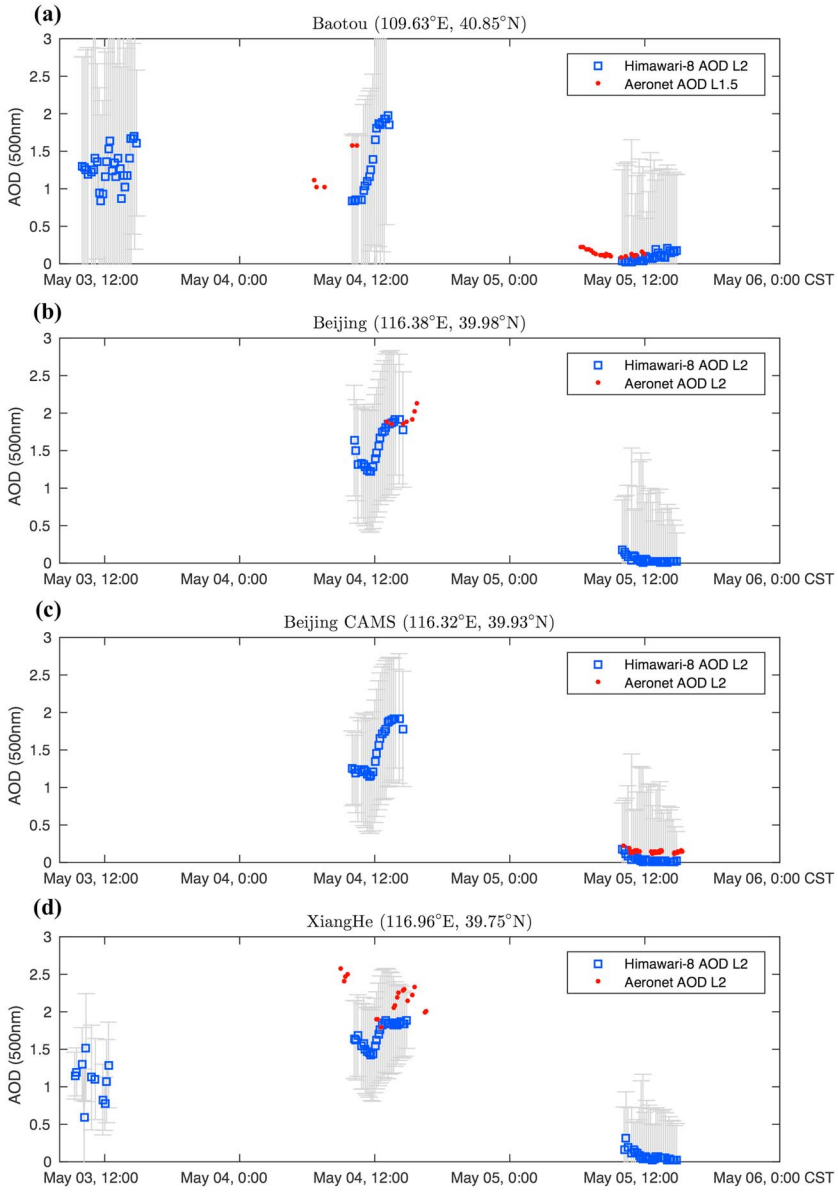

Figure 4. Time series of AOD at or around AERONET sites: AERONET AOD observations (level 1.5 or 2), Himawari-8 AOD retrievals with the gray bar representing the observation error (mean of uncertainties within the grid cell) around the AERONET sites. AERONET = AErosol RObotic NETwork.

spatially smooth and does not contain strong local variability; the impact of observation spatial correlation is then very weak.

5.2. Himawari-8 AOD Versus AERONET

Before assimilating the new Himawari-8 AOD, the product is first evaluated through a comparison to ground-based observations from the AERONET. At the sites of this network, AOD total columns are measured by ground Sun photometers. In the dust-affected region, four AERONET stations are available, marked as A1 to A4 in Figure 6: Baotou, Beijing, Beijing CAMS, and Xianghe. Figure 4 shows the time series of AERONET AOD at these four sites (red marks), either from the Level 1.5 product (cloud screened and quality controlled) or otherwise Level 2.0 (quality assured). Himawari-8 Level 2 AODs at 500 nm are also shown, as average over the 0.25° × 0.25° model grid cell in which the site is located; for each 10-min observation time, the blue mark is the grid cell mean and the gray error bar represents the observation error which is the mean of Himawari AOD uncertainties within the grid cell. As can be seen in the time series, the spread in the Himawari observations is large, but in general, the mean values are rather stable. Though the Himawari

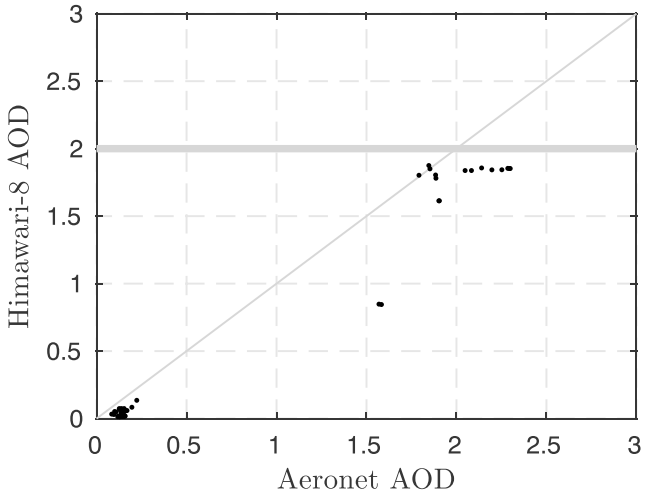

Figure 5. Scatter diagrams of Himawari-8 AOD compared to AERONET AODs at Baotou, Beijing, Beijing CAMS, and XiangHe from 3 to 5 May.

AODs did not match the AERONET measurements all the time, all the AERONET AODs are within the spread of observation error.

On 4 May, high AOD values are observed by AERONET as well as Himawari in all four sites. For the Beijing CAMS station, no observations are available at these moments, but it is supposed to give similar measurements with Beijing and XiangHe due to the small distance. The Himawari AOD observations match well with the AERONET observations during the event. On 5 May, the Himawari and AERONET stations Baotou and Beijing CAMS all observe low AOD values, which indicated the dust storm already expired at that time.

For further comparison, the scatter diagrams of the AODs at the above four sites during the dust storm from 3 to 6 May are plotted in Figure 5. The comparison results in a high correlation coefficient ($R^2 = 0.9762$). As can be seen in the maps before, the Himawari AOD values do not exceed a value of 2; with high dust loads, the AERONET observations reach values in a range of 0.0–2.5. Although this limited comparison is not a guarantee for a high quality of Himawari-8 AODs over the whole model domain in the dust event, the agreement is sufficient to have confidence that this new data set represents the dust plume optical properties.

5.3. Field Station Observations

Since 2013, the China MEP has commenced to release the hourly average measurements of atmospheric constituents including $PM_{2.5}$, PM_{10}, CO, O_3, and SO_2. By now, a network of over 1,500 field stations all over China has been established as shown in Figure 6. Most of these ground stations are located in the densely populated regions in eastern China and are rather far away from the dust source region in Inner Mongolia. Compared to the Himawari-8 AODs, these could not provide information on the dust storm from the very start. However, hourly averaged PM_{10} observations from the network could be used as independent data, to verify the improvement of the dust simulation in the areas where the interest in accurate forecast is the highest.

Though all these Himawari-8, AERONET AODs, and the ground PM_{10} data are actually a sum of the dust aerosols and particles released in local activities, the 2017 dust storm is an extremely severe one; hence, dust aerosols are very dominant in the full aerosols. Therefore, all these measurements are assumed to be consistent to the dust simulations. Observational bias corrections (Dee & Uppala, 2009; Jin et al., 2018) or nondust baseline removals would be required in case of less severe dust storms.

6. Observation Selection for Data Assimilation

The data assimilation system is designed to deal with imperfect model simulations and uncertain observations. For our case, it aims to find the optimum dust emission field that ensures the best match between

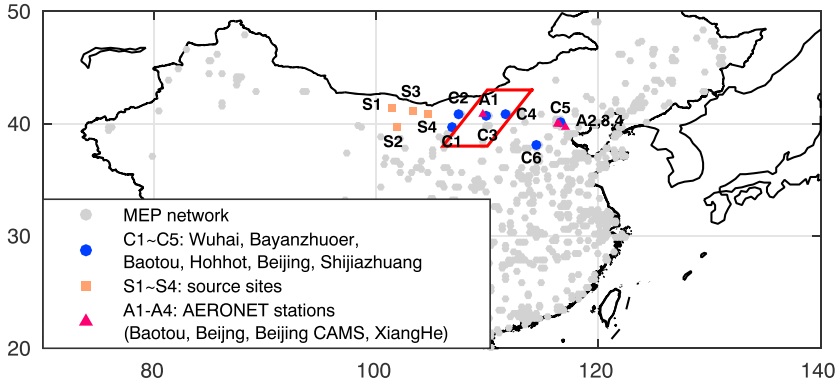

Figure 6. The China MEP network of field measurement stations, AERONET stations, and source region sites. MEP = Ministry of Environmental Protection; AERONET = AErosol RObotic NETwork.

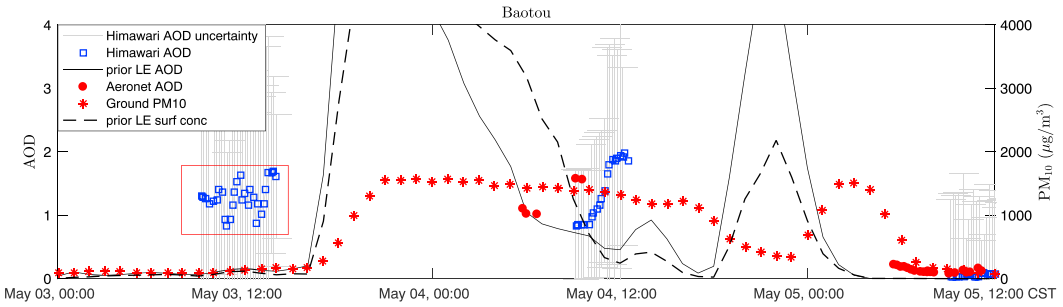

Figure 7. Time series of observed (Himawari-8 and AErosol RObotic NETwork) AOD and simulated AOD (left axis), as well as the observed and simulated surface PM_{10} concentrations in Baotou (right axis).

simulations and Himawari-8 AOD observations. Fundamentally, it relies on the assumptions of an unbiased model and measurements with a Gaussian probability distribution. In practice, the discrepancy between the simulations and the observations can be strongly biased, however, for example, because model errors in deposition and transport are not taken into account. Also, sometimes the AOD retrievals might be strongly biased, for example, due to failed retrievals under the presence of clouds. Such inconsistency will inevitably lead to analysis errors or model divergence.

To limit the negative effects of inconsistency between observations and simulations, algorithms for data selection have been developed and implemented in data assimilation systems (Anderson & Järvinen, 1999; Sakov & Sandery, 2017). The general idea of the observation selection is to exclude measurements that cannot be represented well by the background model simulation. The actually assimilated observations are then a subset of the original data. The reason why certain observations are excluded should be monitored through the assimilation process, and ideally, the assimilation system should be adjusted to allow inclusion of these observations in the future.

6.1. Inconsistence Between the Dust Model and Himawari-8 AODs

Although Figure 1 showed many similarities between the prior LOTOS-EUROS model simulation and the Himawari-8 AOD observations during the dust episode, some significant differences were also found. For instance, on 3 May the Himawari-8 AOD showed high values around the border between Mongolia and Inner Mongolia at 13:00 (CST), marked by the red frame in Figure 1d. However, the model simulated only a small amount of dust there, resulting in modest AOD values. To analyze this discrepancy, the time series of AOD and surface dust concentration in Baotou (located in the highlighted red framework) is shown in Figure 7. The reason to select Baotou is the availability of both Himawari-8 and AERONET AOD observations, as well as a PM_{10} observing site.

Figure 7 shows that the surface PM_{10} observations are low until the arrival of the dust plume around 16:00. The model simulations show the same pattern, but the computed surface dust concentrations are much higher than the actually observed PM_{10} concentrations. The Himawari-8 AOD shows that there are already quite high AOD values around noon. An explanation could be that the dust cloud is initially elevated from the surface and therefore not observed by the PM_{10} network. However, there are no AERONET observations to confirm the heavy dust in the higher vertical layer, which might be an indication that the sky was actually partially clouded as suggested by the RGB composite in Figure 1j. Actually, it is difficult to distinguish between clouds and thick dust especially in those regions where the temporal variations of dust AOD are large, since the Himawari-8 product also uses the temporal variation of observed radiance for the cloud identifications.

The time series in Baotou shows that in this location, for the current model configuration, the simulated surface PM_{10} is strongly correlated with the simulated AOD. Assimilation of the high valued Himawari AOD observations on 3 May would therefore lead to an increase of simulated surface PM_{10}, which is not consistent with the surface observations. Since the high AOD values retrieved from Himawari could not be confirmed by AERONET observations, and might have been caused by a partially clouded scene, it would be better to have these observations excluded from the assimilation. The algorithms of automatic exclusion of these observations, or selection of observations to be used in the assimilation, will be described in sections 6.2 and 6.3, respectively.

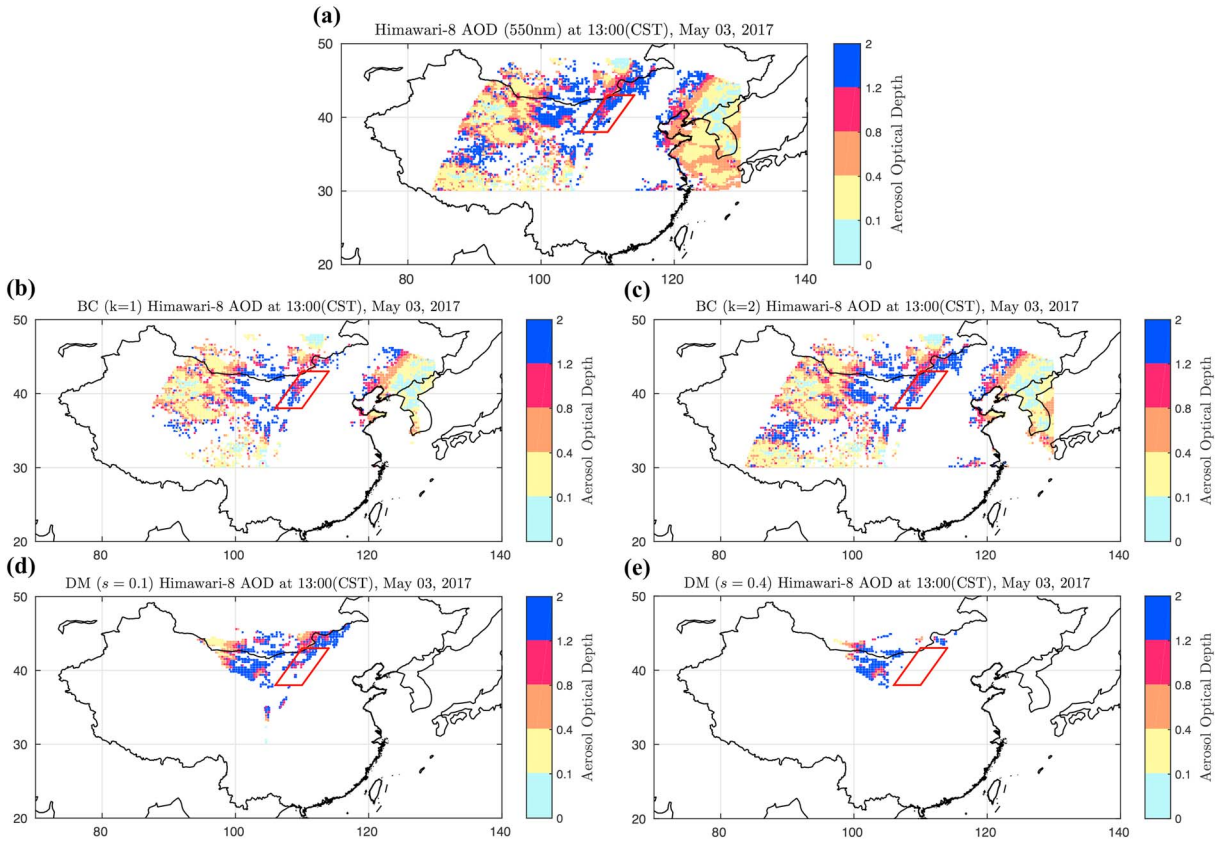

Figure 8. The results of Himawari-8 AOD observations selected for assimilation by the *background check* (BC) and dust mask (DM) criterion at 13:00, 3 May: (a) no selection, (b, c) BC with $\kappa = 1$ and $\kappa = 2$, and (d, e) DM with $s = 0.1$ and $s = 0.4$.

6.2. Background Check

A popular data selection algorithm is the *background check* (BC; Anderson & Järvinen, 1999; Dee et al., 2011). This selects only those observations for which the difference from the background simulation is within a range relative to the uncertainty of the difference

$$\left(\quad y - \mathcal{H}(\mathcal{M}(\vec{f})) \quad \right)^2 \leq \kappa \, (\sigma_b^2 + \sigma_o^2) \tag{15}$$

where the left-hand side represents the square of difference between an observation and the corresponding simulation value by the background model. Under the assumption of this being unbiased, the expected stochastic distribution has zero mean and the variance shown in parentheses at the right-hand side, σ_b and σ_o, are the standard deviations on the diagonals of covariance matrices **B** in the observation space and **R**, respectively. The factor κ is a predefined threshold; a larger κ allows more observations to survive the selection. Anderson and Järvinen (1999) associated quality flags with different values of the threshold, where $\kappa = 0$ selects only *correct* data, $\kappa = 1$ selects *probably correct* data, $\kappa = 2$ also selects *probably incorrect* data, and $\kappa = 3$ even selects *incorrect* data.

Figure 8a shows the coarse AOD from the Himawari data on 3 May 13:00; there are lots of measurements available in the source region, also inside the highlight red frame. Figures 8b and 8c present the selected Himawari-8 AOD using $\kappa = 1$ and $\kappa = 2$ at the same time snapshot. On 3 May, when using a strong selection $\kappa = 1$, many AOD observations are excluded, for example, parts of the observations in red and also many observations in the source regions. Thus, the valuable observations that show the development of the dust storm at an early stage are excluded too. With a more relaxed selection using $\kappa = 2$, more AOD observations in the source region remained but still a lot of them are discarded. Definitely, more AODs in the source region will be kept if a more relaxed BC $\kappa > 2$ is applied, the selection AODs of which are closer to the original observations. On the other hand, observations in the red frame which should have been excluded now remained under these two selections $\kappa = 1$ and $\kappa = 2$. The main reason why these observations are

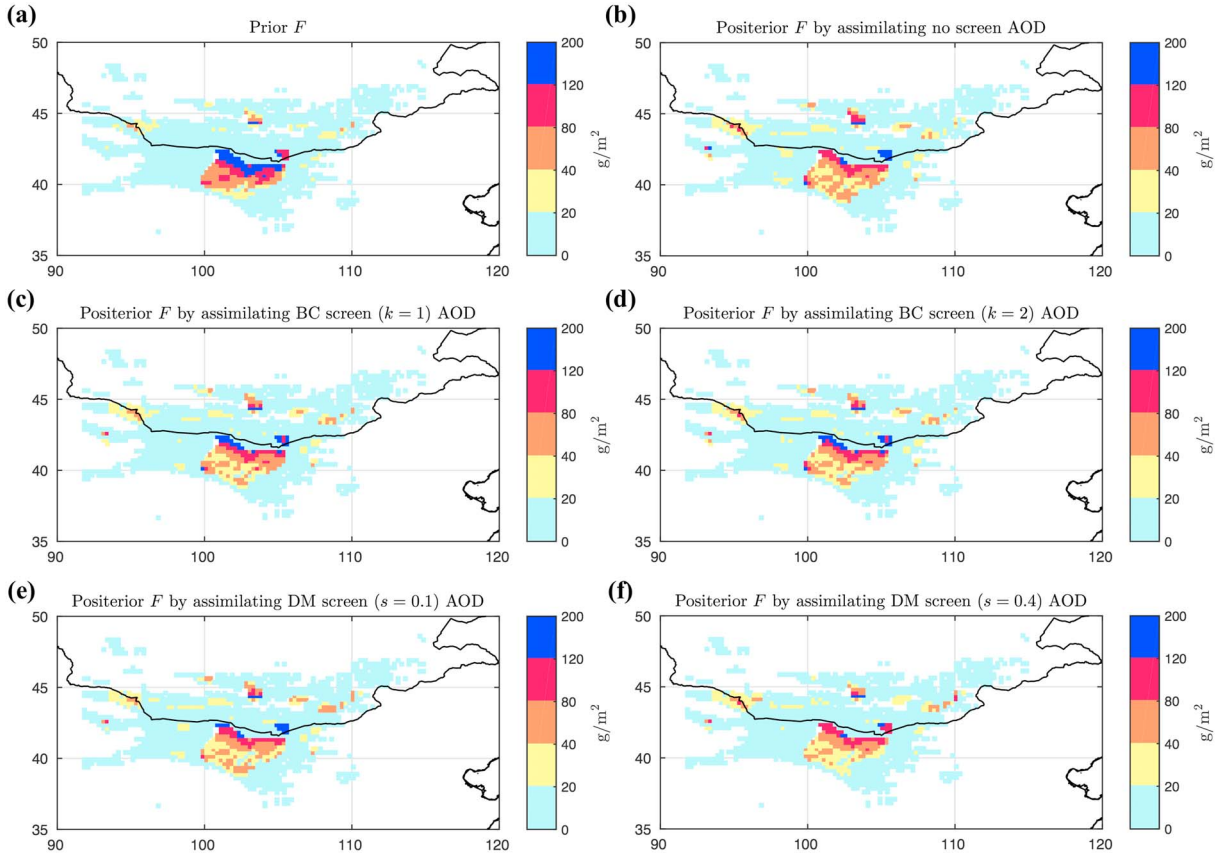

Figure 9. The posterior emission integration index F after the first analysis (15:00, 3 May) using the no screen Himawari-8 (a), BC $k = 1$ (b), $k = 2$ (c), and DM $s = 1$ (d), and $s = 2$ (e) screening methods. BC = background check; DM = dust mask.

selected by the BC is the rather large observation uncertainty, which can be seen in Baotou in Figure 7. On 3 May, the innovations $y - \mathcal{H}(\mathcal{M}(\vec{f})$ are all within the observations' spread of its uncertainty. More restricted selection is then required in order to exclude those unexpected measurements inside marked frame. It is therefore difficult to tune the observation selection properly using this method.

6.3. DM Selection

To have a proper observation selection for the studied application, the DM method is introduced here. The DM criterion selects only those observations in the grid cells where the deterministic model simulation exceeds a certain threshold

$$\mathcal{H}(\mathcal{M}(\vec{f})) \geq s \tag{16}$$

The user defined threshold s denotes a certain dust level over which the grid cell is considered to be affected by the dust storm. The identification of the dust masked region is only based on the initial simulation of the dust model and s and independent of the observation uncertainty. This selection works efficiently in cases where the model is able to reproduce a correct dust plume shape but is not able to simulate the correct amplitude of dust concentrations. The observations are only selected over this dust masked region where the model simulated an amount of dust over this level. In other regions, high AOD values reported by Himawari are excluded, which are due to cloud/dust misdiscrimination or local emissions that are not included in this simulation model. This selection also removes the modest Himawari AODs where the model also produces a low dust level. However, as those measurements are already in good agreements with the model simulations, the exclusion of these data has only minor impacts on the assimilation results.

A limitation of the DM selection is that it could exclude valuable observations in case the model is not able to simulate the dust plume shape correctly. In that case, the model could simulate a modest dust level ($< s$) and hence remove the high AOD values as if they are due to the AOD retrieval error while they actually

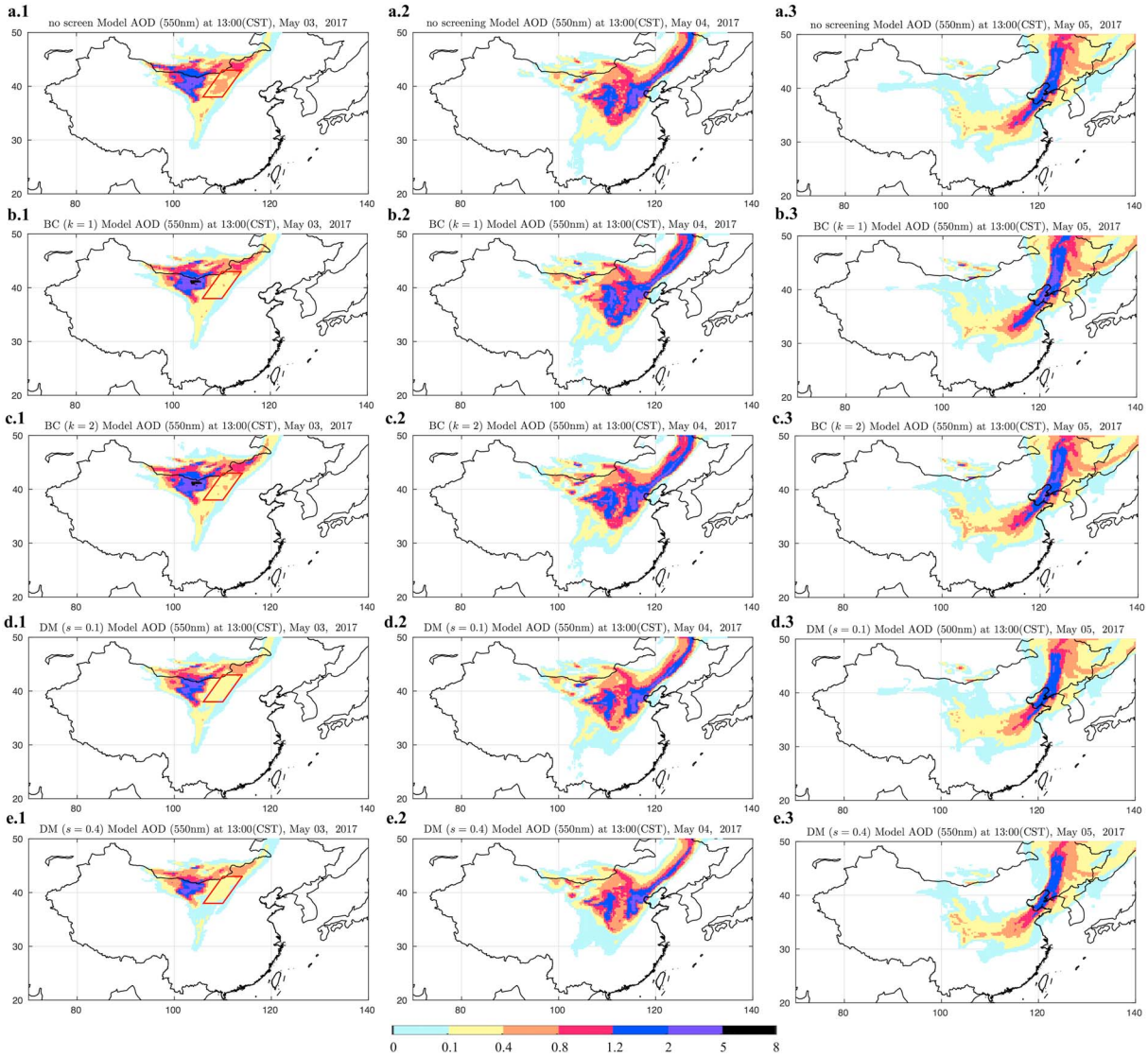

Figure 10. Posterior AOD map using no screen Himawari-8 (a.1–a.3), BC $k = 1$ (b.1–b.3), $k = 2$ (c.1–c.3), and DM $s = 1$ (d.1–d.3), $s = 2$ (e.1–e.3) screening methods at three time snapshots: 13:00 (CST), 3 May (a.1, b.1, c.1, d.1, e.1), 4 May (a.2, b.2, c.2, d.2, e.2), and 5 May (a.3, b.3, c.3, d.3, e.3). Note: the prior model AOD and the Himawari-8 AOD are shown in Figure 1. BC = background check; DM = dust mask.

represent the severe dust. Whether a DM selection is necessary is therefore case dependent and requires inspections of the simulations and AOD observations by the user.

The empirical threshold s is adjustable in practice; if the size of the dust-affected plume is overestimated, a large threshold should be adopted; otherwise, s should be lowered. In our case, we evaluated the impact of the DM threshold by using either $s = 0.1$ or $s = 0.4$, which corresponds to about 5% and 20% of the maximum Himawari AOD value.

Figures 8d and 8e present the Himawari-8 AOD observations selected by the DM criterion, for two different thresholds $s = 0.4$ and $s = 0.1$. When using a high DM threshold $s = 0.4$, the dust-affected region is located exactly in the source region; observations outside are all excluded. With a lower threshold $s = 0.1$, a larger dust-affected region is identified, observations near the source region are also selected. Moreover, all observations inside the highlighted red frame are excluded with $s = 0.4$ since the background model shows that the dust level there is very low (< 0.4), and a small portion of these data are kept in case a lower threshold $s = 0.1$ is set.

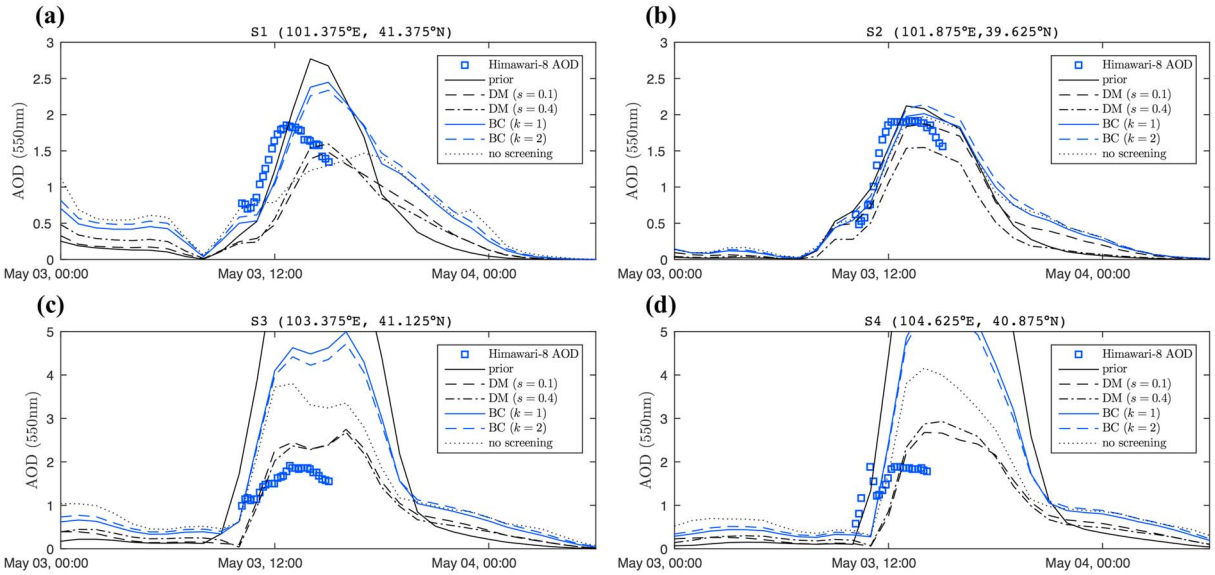

Figure 11. Time series of AOD in four sites in the source region site on 3 May, (Himawari observations averaged over the 0.25 × 0.25 model grid). DM = dust mask; BC = background check.

7. Result and Discussion

7.1. Emission Analysis

Using the above described configurations, the Himawari-8 AOD observations have been assimilated for the dust storm event to estimate the dust emission field $\vec{f}$. Different assimilation runs were performed, either using all observations or using a subset of AODs selected by the BC or DM. Figures 9a–9f show the map of prior, several posterior emission integration index F (the definition can be found in section 3.5) over the potential source region during the period of the two assimilation windows. The prior model simulated the highest emission integration, especially in the boundary region between China and Mongolia. In a large number of grid cells, the accumulated dust emissions are in the range from 120 to 200 g/m^2, which resulted in the overestimation of the AODs in dust plume center as can be seen in Figure 1a. The assimilation of all available Himawari AODs and DM selected AODs generally computed a lower level of dust emission; there are only a few grid cells with the integrated emission exceeding 120 g/m^2.

As mentioned in section 6.2, many of the AOD observations in the source region are excluded while using the BC selection, because they exceed the uncertainty spread of simulation-observation difference in equation (14). Although the estimated emissions also decreased a bit, the emission flux F still stayed at a much higher level than posterior emissions by assimilating raw AODs and DM screened AODs.

7.2. AOD Analysis

In each experiment, the LOTOS-EUROS model is used to simulate the dust load using the optimized dust emissions, and both column-integrated AOD and surface PM_{10} are evaluated with observations.

Figures 10a–10e show the snapshots of AODs over the domain for each of the 3 days of the events, either using all observations or parts of AODs from a selection. The prior model AODs at these three corresponding moments are plotted in Figures 1a–1c, while the original Himawari-8 AODs are shown in Figures 1d–1f. The simulated AOD values show in general the same patterns as the observations for all experiments, but differences are present at regional scale. Compared to the background simulation, in which the model AODs are significantly overestimated at the center of the dust plume, all the posterior AODs decreased after assimilation, but different assimilation runs also resulted in different increments.

The effect of the different observation selection criteria is best seen on 3 May for the area marked by the red frame. If no selection is applied and all observations are used in the assimilation, emissions are elevated to a level which is able to produce high simulated AOD values in the red marked region. When a BC selection is applied (Figures 10b–10c), the simulated AODs are lower in the marked area as parts of the high-value AODs are excluded. However, since this BC also excluded observations over the source region, the assimilation is less effective to change the dust emissions here and the simulated AOD remains rather high (values above 5).

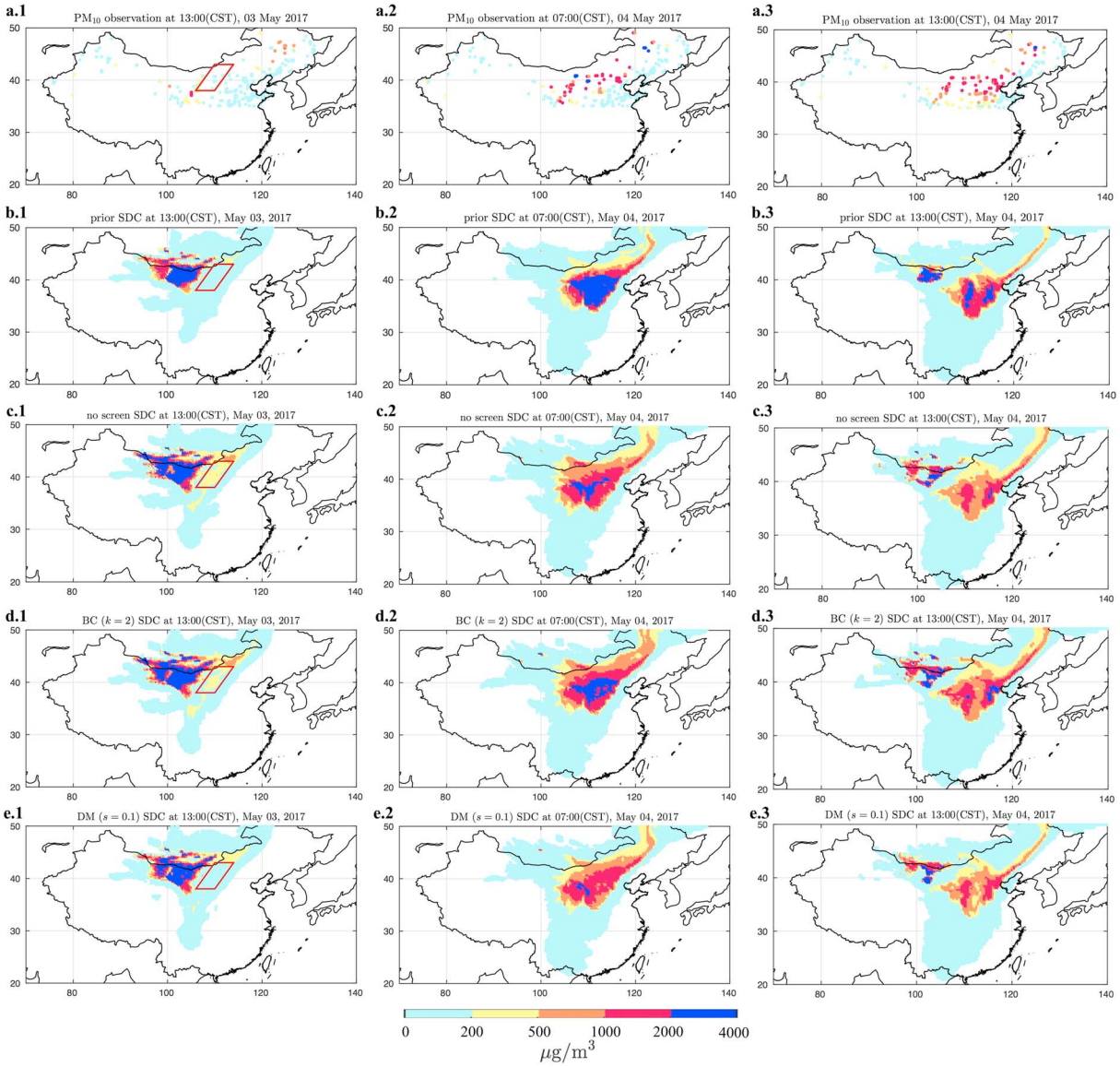

Figure 12. Field PM_{10}, prior and posterior surface dust concentration (SDC) map at 13:00, 3 May (a.1–e.1); 07:00, 4 May (a.1–e.1); and 13:00, 4 May (a.1–e.1). BC = background check; DM = dust mask.

This effect is less strong when a more relaxed selection ($\kappa = 2$) is performed, which also leads to higher AOD values in the marked area. When the DM criteria are used (Figures 10d and 10e), the simulated AODs in the marked area remain low and are better than the results obtained using the BC. In addition, the simulated high AOD values in the source region are also tuned to a low level which are in better agreement with the observations. In similar cases, the predefined DM threshold s is recommended to be set from 5% to 20% of the maximum AOD value; a too high threshold will exclude most observations, while a too low value makes the observation selection less effective.

To illustrate the differences in the posterior AOD performance for the different selection criteria, Figure 11 shows the time series of AOD at four locations in the source region (S1–S4 in Figure 6) during the evolution of the dust storm on 3 May. The strong dust emissions occurred on this day in this region, and the Himawari-8 observations are also available. In S1 and S2, the prior model already produced an AOD simulation that is close to the Himawari-8 AOD; however, the model strongly overestimated the AODs in S3 and S4. This suggests that the existing emission parametrization is in principle able to simulate dust loads, but at local scale the error might still be large. Assimilation using all available observations (no selection) strongly improves the simulation, and the best results are obtained using the DM selection criteria. Selection based

on BC leads to simulations with still much too high AOD, since many of the AOD observations in the source region are actually not selected for assimilation.

The impact of the different observation selection on the AOD simulation can also be observed on 4 May in Figures 10a.2–10e.2. If no selections are performed, the simulated AOD values are still a bit overestimated in the plume center; also, the size of dust-affected region ($AOD > 0.1$) is extended compared to the background simulation. When the BC is implemented, the dust-affected region is limited because parts of the inconsistent data are excluded. However, the simulated AOD is still significantly overestimated in the plume center due to the exclusion of the AOD observations in the source region in the first cycle. In the cases when DM selection is applied, the size of the dust plume is not much extended especially when a restricted selection $s = 0.4$ is used, and the AOD simulation overestimation is mitigated.

On 5 May, differences in the of simulated AODs using the two observation selections still existed but were not so strong.

7.3. Comparison With Surface PM_{10}

In order to further evaluate the posterior simulations, the simulations of PM_{10} are now compared with observations from the surface network described in section 5.3. Since these observations were not assimilated, this assessment will show the added value of assimilation the Himawari AOD for surface PM_{10} concentrations.

It should be noted that the PM_{10} observations represent not only the dust aerosols but also the particulate matters from local anthropogenic activities. In most cities, the PM_{10} values are in a range of 10–200 $\mu g/m^3$ during the nondust period. During a dust event, however, the maximum PM_{10} concentrations easily reach several thousands $\mu g/m^3$. Therefore, in this study the PM_{10} observations are compared directly with the simulated total dust concentrations, neglecting that a small part of the observations is actually nondust and without using any nondust aerosol correction. Besides, we only used the PM_{10} from the 200 sites in the North China which reported this severe dust phenomena instead of assimilating all measurements, since some sites in the South China were free of the dust during the episode. Figures 12a–12e show the three time snapshots of surface PM_{10}, from the observation network or from the background simulation or from the posterior simulations using different AOD selections. These three snapshots show the whole process of the dust transport. On 3 May 13:00 (CST), the first high surface PM_{10} concentrations are observed around the Mongolia and Gobi Deserts. The plume then moves to the Central and Northeast China and leads to significantly increased concentrations in the morning of 4 May 7:00, and severe dust plume is further carried southeastward and the surface dust concentrations stayed at a very high level in the following 6 hr. In the time followed, the surface dust concentrations start to decrease gradually and are much weaker compared to the ones at 4 May, 07:00 and 13:00, and are not shown here.

Figure 12a.1 shows that most of the surface sites are free of extreme dust loads on 3 May 13:00 (CST), and the PM_{10}s are below 200 $\mu g/m^3$ (first row). Figure 12c.1 shows the map with the posterior dust concentrations obtained by assimilating all Himawari-8 AOD (third row). Unlike the observed PM_{10} map, it shows that there are also nonnegligible dust concentrations of about 200–500 $\mu g/m^3$, especially inside the red frame. Similarly, the assimilation of the BC selected observations (fourth row) also shows high level dust concentrations in the marked area since the BC selection did not exclude the high AOD values there. On the contrary, both the prior concentrations (second row) and the assimilations using DM observation selection (fifth row) do not show high PM loads in this region. This shows that assimilation of certain observations introduces unrealistic dust concentrations at the surface.

Figures 12a.2–12a.3 show the surface PM_{10} concentrations at the other two snapshots on 4 May 7:00 and 13:00. Severe dust concentrations are reported by stations all over North China, with a few values up to 2,000 $\mu g/m^3$, and most ones stay in a range of 500 to 2,000 $\mu g/m^3$. The second row shows the corresponding background simulations. Similar to the AOD, the background simulation also overestimated the PM_{10}, and at many locations the simulated concentrations exceed 2,000 $\mu g/m^3$. The assimilation of Himawari AOD (third to fifth row) lowers the concentrations, where the best result is seen when DM selection is used. When the DM selection is performed, the estimated surface concentrations are now in a range of 500 to 2,000 $\mu g/m^3$, which is in agreement with the observations.

To further analyze the performance in simulations of surface concentrations, the time series of surface dust concentration in six sites and the ground PM_{10} measurements are shown in Figure 13. The locations of these six sites can be found in Figure 6.

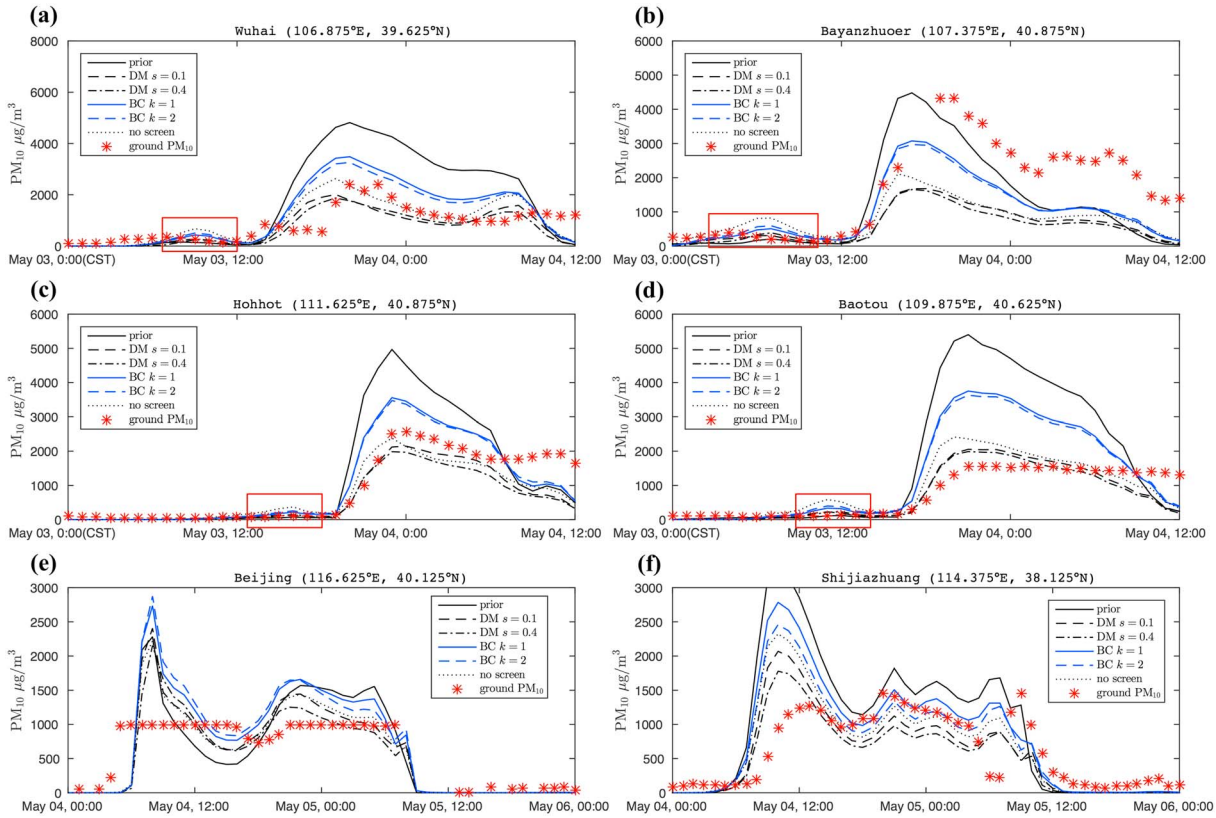

Figure 13. Time series of PM_{10} and surface dust concentration in C1 to C6:(C1: Wuhai, C2: Bayanzhuoer, C3: Wuhai, C4: Baotou, C5: Beijing, and C6: Shijiazhuang). DM = dust mask; BC = background check.

The PM_{10} observations indicate that the dust storm arrived in Wuhai and Bayanzhuoer on 3 May around 14:00 and in Hohhot and Baotou around 19:00. The time series of the prior simulation follow this pattern, although the simulated values are 2 to 3 times higher than the observed.

After assimilation of Himawari-8 AODs, the posterior concentrations are strongly improved in Wuhai, Hohhot and Baotou, as shown in Figures 13a, 13c, and 13d. Best results are obtained when the DM selection is applied. The assimilation does not improve concentrations in Bayanzhuoer as shown in Figure 13b; the observations there reach values as high as 4,000 $\mu g/m^3$, while the maximum simulated concentrations after assimilation are around 1,500 $\mu g/m^3$.

Assimilation of all available data or using the BC selection criteria could introduce a small inconsistency in the surface concentrations in the early morning of 3 May, as indicated by the red boxes in Figures 13a–13d. In some assimilations an extra peak in the dust concentrations is incurred, with a maximum around 200 to 500 $\mu g/m^3$. This peak was caused by the assimilation of AOD observations that cannot be represented correctly by the model; it still exists in the assimilation when BC is performed but can be eliminated when the DM selection is applied.

In the two downstream sites Beijing and Shijiazhuang, the dust plume only arrives in the morning of 4 May. The model is able to simulate the arrival and departure of the plume correctly. The amplitude of the concentrations is too high for the background simulation, although this is not completely sure for the Beijing site since observations seem to be limited to 1,000 $\mu g/m^3$. After assimilation the model simulations are in better agreement with the observations in especially Shijiazhuang, with best results obtained using the DM selection.

7.4. Forecast Skill

A practical application of the AOD assimilation is to serve as the start of a forecast. This could be used to timely provide information to the public on the arrival of the dust plume and the expected dust concentrations.

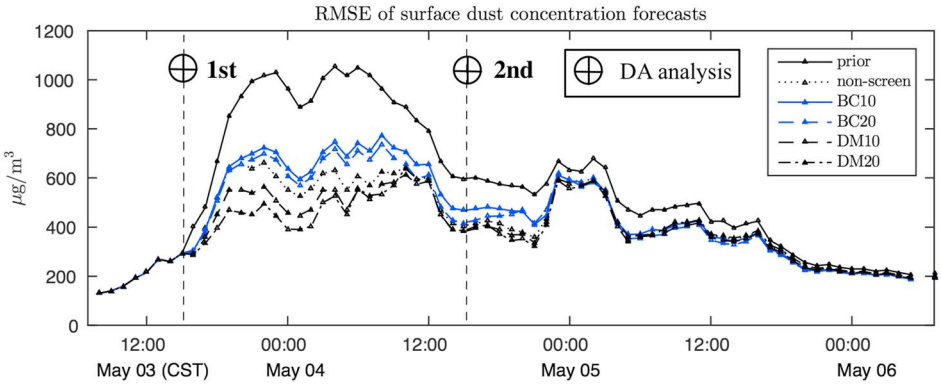

Figure 14. Time series of the RMSE of the model surface dust concentration forecasts with respect to the field measurements of PM_{10}. RMSE = root-mean-square error; BC = background check; DM = dust mask.

To evaluate the forecast skill, the hourly root-mean-square error (RMSE) between observed and simulated surface PM_{10} has been computed over the 200 northern stations most affected by the dust. As shown in Figure 14, the first and second data assimilation analyses are performed on 3 May 15:00 and 4 May 15:00, respectively. Each hourly forecasts before the first analysis is provided by the background model, forecasts from 3 May 15:00 to 4 May 15:00 are based on the estimated emission from the first analysis, while forecasts in the following hours are based on the optimized emission from the second analysis. Therefore, all the surface PM_{10} simulations here could be used as the forecasts in the dust early warning system. Figure 14 shows a time series of the RMSE values. Before the first assimilation analysis is conducted, all the forecasts are based on the background emission and show the same performance. Though our prior model already provides a good temporal match of real dust event, the discrepancy is still large due to difficulty in accurately modeling the actual dust levels. A consistent improvement of the dust forecast skill is shown when the data assimilation is implemented. The maximum RMSE around 4 May 0:00 is reduced from 1,000 to 600 $\mu g/m^3$ when the forecast is based on assimilated dust emissions; the forecast skill is further improved with RMSE values reduced to 500 $\mu g/m^3$ if the dust mask selection is applied. When the BC is used for observation selection, RMSE values are actually higher than in the case with all observations included.

8. Conclusions

In this study, a dust emission inverse modeling system was developed. Total column AOD observations from the new geostationary satellite Himawari-8 have been used to correct mismatches in the dust emission parametrization. Its aerosol product has a wide spatial coverage and high spatial and temporal resolution, which provides valuable information to monitor dust storms over Asia.

An extreme dust storm event over North China during 3–5 May 2017 was selected as test case for the assimilation. For this event, the Himawari-8 AOD observations were found to be consistent with the available AOD observations from the AERONET network. Simulations of dust have been made using the LOTOS-EUROS regional air quality model, and time series of simulated AOD showed in general good agreements with the observations with respect to arrival and decrease of the dust storm, but the amplitude is over estimated.

In one region the satellite retrievals of AOD showed rather high values that are not represented by the simulation model. These high AOD values could not be confirmed by AERONET observations and might be attributed to the presence of the partially clouded scenes. Using these Himawari observations in an assimilation would then lead to analyzed dust emissions that further result in incorrect simulations. Therefore, observation selection criteria have been developed by selecting only those observations that can be represented by the model. A DM selection that uses only those observations, where the model also simulates an amount of dust, was shown to provide the best results.

The assimilation system uses a RTL 4DVar technique to estimate dust emissions over daily time windows during the dust event. Both uncertainties in the meteorological wind field and the friction velocity threshold field are taken into account when the emission uncertainty is approximated. Assimilation of Himawari AOD is shown to provide emission estimates that, when used as input for the model, strongly improves

the simulated AOD as well as the simulated surface concentrations compared to the PM_{10} observations. Using proper selection of AOD observations in the assimilation, the forecast skill during the dust storm was strongly improved.

Acknowledgments
The research product of aerosol properties (produced from Himawari-8) that was used in this paper was derived by the algorithm developed by Japan Aerospace Exploration Agency (JAXA) and the National Institute of Environmental Studies (NIES) and available at https://www.eorc.jaxa.jp/ptree/. The ground-based aerosol properties are from the AErosol RObotic NETwork and are available at https://aeronet.gsfc.nasa.gov/. The real-time PM_{10} data are from the network established by the China Ministry of Environmental Protection and accessible to the public at http://106.37.208.233:20035/. One can also access the historic profile by visiting http://www.aqistudy.cn/.

References

Anderson, E., & Järvinen, H. (1999). Variational quality control. *Quarterly Journal of the Royal Meteorological Society*, *125*(554), 697–722. https://doi.org/10.1002/qj.49712555416

Arnoldi, W. E. (1951). The principle of minimized iterations in the solution of the matrix eigenvalue problem. *Quarterly of Applied Mathematics*, *9*(1), 17–29.

Bessho, K., Date, K., Hayashi, M., Ikeda, A., Imai, T., Inoue, H., et al. (2016). An introduction to Himawari-8/9—Japan's new-generation geostationary meteorological satellites. *Journal of the Meteorological Society of Japan. Ser. II*, *94*(2), 151–183. https://doi.org/10.2151/jmsj.2016-009

Calil, P. H. R., Doney, S. C., Yumimoto, K., Eguchi, K., & Takemura, T. (2011). Episodic upwelling and dust deposition as bloom triggers in low-nutrient, low-chlorophyll regions. *Journal of Geophysical Research*, *116*, C06030. https://doi.org/10.1029/2010jc006704

Carrer, D., Roujean, J.-L., Hautecoeur, O., & Elias, T. (2010). Daily estimates of aerosol optical thickness over land surface based on a directional and temporal analysis of SEVIRI MSG visible observations. *Journal of Geophysical Research*, *115*, D10208. https://doi.org/10.1029/2009JD012272

Cesnulyte, V., Lindfors, A. V., Pitkänen, M. R. A., Lehtinen, K. E. J., Morcrette, J. J., & Arola, A. (2014). Comparing ECMWF AOD with AERONET observations at visible and UV wavelengths. *Atmospheric Chemistry and Physics*, *14*(2), 593–608.

Dee, D. P., & Uppala, S. (2009). Variational bias correction of satellite radiance data in the ERA-Interim reanalysis. *Quarterly Journal of the Royal Meteorological Society*, *135*(644), 1830–1841. https://doi.org/10.1002/qj.493

Dee, D. P., Uppala, S. M., Simmons, A. J., Berrisford, P., Poli, P., Kobayashi, S., et al. (2011). The ERA-Interim reanalysis: Configuration and performance of the data assimilation system. *Quarterly Journal of the Royal Meteorological Society*, *137*, 553–597. https://doi.org/10.1002/qj.828

Di Tomaso, E., Nick, Jorba, O., & Garcia-Pando, C. P. (2017). Assimilation of MODIS dark target and deep blue observations in the dust aerosol component of NMMB-MONARCH version 1.0. *Geoscientific Model Development*, *10*, 1107–1129.

Escribano, J., Boucher, O., Chevallier, F., & Huneeus, N. (2016). Subregional inversion of North African dust sources. *Journal of Geophysical Research: Atmospheres*, *121*, 8549–8566. https://doi.org/10.1002/2016JD025020

Foroutan, H., & Pleim, J. E. (2017). Improving the simulation of convective dust storms in regional-to-global models. *Journal of Advances in Modeling Earth Systems*, *9*, 2046–2060. https://doi.org/10.1002/2017MS000953

Foroutan, H., Young, J., Napelenok, S., Ran, L., Appel, K. W., Gilliam, R. C., & Pleim, J. E. (2017). Development and evaluation of a physics-based windblown dust emission scheme implemented in the CMAQ modeling system. *Journal of Advances in Modeling Earth Systems*, *9*, 585–608. https://doi.org/10.1002/2016MS000823

Fu, G., Prata, F., Lin, H. X., Heemink, A., Segers, A., & Lu, S. (2017). Data assimilation for volcanic ash plumes using a satellite observational operator: A case study on the 2010 Eyjafjallajokull volcanic eruption. *Atmospheric Chemistry and Physics*, *17*(2), 1187–1205.

Fukuda, S., Nakajima, T., Takenaka, H., Higurashi, A., Kikuchi, N., Nakajima, T. Y., & Ishida, H. (2013). New approaches to removing cloud shadows and evaluating the 380 nm surface reflectance for improved aerosol optical thickness retrievals from the GOSAT/TANSO-Cloud and Aerosol Imager. *Journal of Geophysical Research: Atmospheres*, *118*, 13,520–13,531. https://doi.org/10.1002/2013jd020090

Gong, S. L., & Zhang, X. Y. (2008). CUACE/Dust—An integrated system of observation and modeling systems for operational dust forecasting in Asia. *Atmospheric Chemistry and Physics*, *8*(9), 2333–2340. https://doi.org/10.5194/acp-8-2333-2008

Gong, S. L., Zhang, X. Y., Zhao, T. L., McKendry, I. G., Jaffe, D. A., & Lu, N. M. (2003). Characterization of soil dust aerosol in China and its transport and distribution during 2001 ACE-Asia: 2. Model simulation and validation. *Journal of Geophysical Research*, *108*(D9), 4262. https://doi.org/10.1029/2002jd002633

Huneeus, N., Schulz, M., Balkanski, Y., Griesfeller, J., Prospero, J., Kinne, S., et al. (2011). Global dust model intercomparison in AeroCom phase I. *Atmospheric Chemistry and Physics*, *11*(15), 7781–7816. https://doi.org/10.5194/acp-11-7781-2011

Ian, A., & Richard, W. (2012). An automated dust detection using SEVIRI: A multiyear climatology of summertime dustiness in the central and western Sahara. *Journal of Geophysical Research*, *117*, D08202. https://doi.org/10.1029/2011JD016845

Ishida, H., & Nakajima, T. Y. (2009). Development of an unbiased cloud detection algorithm for a spaceborne multispectral imager. *Journal of Geophysical Research*, *114*, D07206. https://doi.org/10.1029/2008jd010710

Jin, J., Lin, H. X., Heemink, A., & Segers, A. (2018). Spatially varying parameter estimation for dust emissions using reduced-tangent-linearization 4DVar. *Atmospheric Environment*, *187*, 358–373.

Khade, V. M., Hansen, J. A., Reid, J. S., & Westphal, D. L. (2013). Ensemble filter based estimation of spatially distributed parameters in a mesoscale dust model: Experiments with simulated and real data. *Atmospheric Chemistry and Physics*, *13*(6), 3481–3500.

Lin, C., Wang, Z., & Zhu, J. (2008a). An ensemble Kalman filter for severe dust storm data assimilation over China. *Atmospheric Chemistry & Physics*, *8*, 2975–2983.

Lin, C., Zhu, J., & Wang, Z. (2008b). Model bias correction for dust storm forecast using ensemble Kalman filter. *Journal of Geophysical Research*, *113*, D14306. https://doi.org/10.1029/2007jd009498

Liu, M., Westphal, D. L., Wang, S., Shimizu, A., Sugimoto, N., Zhou, J., & Chen, Y. (2003). A high-resolution numerical study of the Asian dust storms of April 2001. *Journal of Geophysical Research*, *108*(D23), 8653. https://doi.org/10.1029/2002jd003178

Manders, A. M. M., Builtjes, P. J. H., Curier, L., Denier van der Gon, H. A. C., Hendriks, C., Jonkers, S., et al. (2017). Curriculum vitae of the LOTOS-EUROS (v2.0) chemistry transport model. *Geoscientific Model Development*, *10*(11), 4145–4173.

Marticorena, B., & Bergametti, G. (1995). Modeling the atmospheric dust cycle: 1. Design of a soil-derived dust emission scheme. *Journal of Geophysical Research*, *100*(D8), 16,415–16,430. https://doi.org/10.1029/95JD00690

Mona, L., Papagiannopoulos, N., Basart, S., Baldasano, J., Binietoglou, I., Cornacchia, C., & Pappalardo, G. (2014). EARLINET dust observations vs. BSC-DREAM8b modeled profiles: 12-year-long systematic comparison at Potenza, Italy. *Atmospheric Chemistry and Physics*, *14*(16), 8781–8793.

Niu, T., Gong, S. L., Zhu, G. F., Liu, H. L., Hu, X. Q., Zhou, C. H., & Wang, Y. Q. (2008). Data assimilation of dust aerosol observations for the CUACE/dust forecasting system. *Atmospheric Chemistry and Physics*, *8*(13), 3473–3482. https://doi.org/10.5194/acp-8-3473-2008

Remer, L. A., Kaufman, Y. J., Tanré, D., Mattoo, S., Chu, D. A., Martins, J. V., et al. (2005). The MODIS aerosol algorithm, products, and validation. *Journal of the Atmospheric Sciences*, *62*(4), 947–973.

Sakov, P., & Sandery, P. (2017). An adaptive quality control procedure for data assimilation. *Tellus A: Dynamic Meteorology and Oceanography*, *69*(1), 1318031. https://doi.org/10.1080/16000870.2017.1318031

Schutgens, N., Nakata, M., & Nakajima, T. (2012). Estimating aerosol emissions by assimilating remote sensing observations into a global transport model. *Remote Sensing*, *4*(11), 3528–3543. https://doi.org/10.3390/rs4113528

Sekiyama, T. T., Tanaka, T. Y., Shimizu, A., & Miyoshi, T. (2010). Data assimilation of CALIPSO aerosol observations. *Atmospheric Chemistry and Physics*, *10*(1), 39–49.

Sekiyama, T. T., Yumimoto, K., Tanaka, T. Y., Nagao, T., Kikuchi, M., & Murakami, H. (2016). Data assimilation of Himawari-8 aerosol observations: Asian dust forecast in June 2015. *SOLA*, *12*, 86–90.

Shao, Y. P., & Dong, C. H. (2006). A review on East Asian dust storm climate, modelling and monitoring. *Global and Planetary Change*, *52*(1-4), 1–22. https://doi.org/10.1016/j.gloplacha.2006.02.011

Shao, Y. P., Raupach, M. R., & Leys, J. F. (1996). A model for predicting aeolian sand drift and dust entrainment on scales from paddock to region. *Australian Journal of Soil Research*, *34*(3), 309–342. https://doi.org/10.1071/sr9960309

Timmermans, R., Kranenburg, R., Manders, A., Hendriks, C., Segers, A., Dammers, E., et al. (2017). Source apportionment of PM2.5 across China using LOTOS-EUROS. *Atmospheric Environment*, *164*, 370–386. https://doi.org/10.1016/j.atmosenv.2017.06.003

Uno, I., Wang, Z., Chiba, M., Chun, Y. S., Gong, S. L., Hara, Y., et al. (2006). Dust model intercomparison (DMIP) study over Asia: Overview. *Journal of Geophysical Research*, *111*, D12213. https://doi.org/10.1029/2005jd006575

Wang, Z., Ueda, H., & Huang, M. (2000). A deflation module for use in modeling long-range transport of yellow sand over East Asia. *Journal of Geophysical Research*, *105*(D22), 26,947–26,959. https://doi.org/10.1029/2000jd900370

Wang, Y. Q., Zhang, X. Y., Gong, S. L., Zhou, C. H., Hu, X. Q., Liu, H. L., et al. (2008). Surface observation of sand and dust storm in East Asia and its application in CUACE/Dust. *Atmospheric Chemistry and Physics*, *8*(3), 545–553. https://doi.org/10.5194/acp-8-545-2008

Wu, C., Lin, Z., He, J., Zhang, M., Liu, X., Zhang, R., & Brown, H. (2016). A process-oriented evaluation of dust emission parameterizations in CESM: Simulation of a typical severe dust storm in East Asia. *Journal of Advances in Modeling Earth Systems*, *8*, 1432–1452. https://doi.org/10.1002/2016MS000723

Yoshida, M., Kikuchi, M., Nagao, T. M., Murakami, H., Nomaki, T., & Higurashi, A. (2018). Common retrieval of aerosol properties for imaging satellite sensors. *Journal of the Meteorological Society of Japan. Ser. II*, *96B*, 133.

Yumimoto, K., Murakami, H., Tanaka, T. Y., Sekiyama, T. T., Ogi, A., & Maki, T. (2016). Forecasting of Asian dust storm that occurred on May 10-13, 2011, using an ensemble-based data assimilation system. *Particuology*, *28*, 121–130. https://doi.org/10.1016/j.partic.2015.09.001

Yumimoto, K., Nagao, T. M., Kikuchi, M., Sekiyama, T. T., Murakami, H., Tanaka, T. Y., et al. (2016). Aerosol data assimilation using data from Himawari-8, a next-generation geostationary meteorological satellite. *Geophysical Research Letters*, *43*, 5886–5894. https://doi.org/10.1002/2016gl069298

Yumimoto, K., & Takemura, T. (2015). Long-term inverse modeling of Asian dust: Interannual variations of its emission, transport, deposition, and radiative forcing. *Journal of Geophysical Research: Atmospheres*, *120*, 1582–1607. https://doi.org/10.1002/2014jd022390

Yumimoto, K., Uno, I., Sugimoto, N., Shimizu, A., Liu, Z., & Winker, D. M. (2008). Adjoint inversion modeling of Asian dust emission using lidar observations. *Atmospheric Chemistry and Physics*, *8*(11), 2869–2884. https://doi.org/10.5194/acp-8-2869-2008

Zhang, Z., Wu, W., Fan, M., Tao, M., Wei, J., Jin, J., et al. (2019). Validation of Himawari-8 aerosol optical depth retrievals over China. *Atmospheric Environment*, *199*(1352-2310), 32–44.

Zhou, C. H., Gong, S. L., Zhang, X. Y., Wang, Y. Q., Niu, T., Liu, H. L., et al. (2008). Development and evaluation of an operational SDS forecasting system for East Asia: CUACE/Dust. *Atmospheric Chemistry and Physics*, *8*(4), 787–798. https://doi.org/10.5194/acp-8-787-2008